

Incorporating the effect of small-scale circulations upon dust emission in an atmospheric general circulation model

R. V. Cakmur and R. L. Miller

Department of Applied Physics and Applied Mathematics, Columbia University, New York, New York, USA

NASA Goddard Institute for Space Studies, New York, New York, USA

O. Torres

Joint Center for Earth Systems Technology, University of Maryland, Baltimore County, Baltimore, Maryland, USA

Received 12 August 2003; revised 13 November 2003; accepted 13 January 2004; published 1 April 2004.

[1] Realistic simulation of dust emission in an atmospheric general circulation model (AGCM) is inhibited by the model's coarse resolution compared to the scale of the circulations observed to mobilize dust. We construct a probability distribution of wind speed within each grid box that depends upon the speed explicitly calculated by the AGCM and the magnitude of fluctuations about this speed. This magnitude is calculated by incorporating information from the AGCM's parameterizations of the planetary boundary layer along with dry and moist convection. Emission depends on the fraction of the wind speed distribution above the threshold value. As a consequence, emission can occur even if the explicitly resolved wind speed is less than the threshold, as long as the subgrid scale variability is large enough. In the AGCM, subgrid wind fluctuations are dominated by dry convection. This favors dust emission over deserts, where there is continuous mixing within the boundary layer due to intense solar heating of the surface. Particles emitted over arid regions are farther from precipitation and mixed higher above the surface by dry convection. This increases their wet and dry deposition lifetimes, respectively, increasing the aerosol load for a given emission. The AGCM's identification of "preferred meteorology" for emission by subgrid circulations complements the preferred sources of erodible particles included in other models. Given the introduction of subgrid variability, the AGCM's dust aerosol burden improves significantly, compared to the Total Ozone Mapping Spectrometer (TOMS) and advanced very high resolution radiometer (AVHRR) aerosol optical thickness (AOT) retrievals, over the Sahara, Sahel, and the Taklimakan as well as downwind of these regions, considered to be major sources of dust emission. This mechanistic representation of subgrid variability allows us to calculate the atmospheric burden of dust under different climates, where emission can change due to altered boundary layer variability in addition to changes in the mean wind speed.

INDEX TERMS: 0305 Atmospheric Composition and Structure: Aerosols and particles (0345, 4801); 0322 Atmospheric Composition and Structure: Constituent sources and sinks; 3322 Meteorology and Atmospheric Dynamics: Land/atmosphere interactions; 3307 Meteorology and Atmospheric Dynamics: Boundary layer processes; **KEYWORDS:** dust modeling

Citation: Cakmur, R. V., R. L. Miller, and O. Torres (2004), Incorporating the effect of small-scale circulations upon dust emission in an atmospheric general circulation model, *J. Geophys. Res.*, 109, D07201, doi:10.1029/2003JD004067.

1. Introduction

[2] Dust emission occurs over dry soils when the wind speed exceeds a certain threshold [Gillette, 1978]. Given the cubic dependence of emission upon wind speed, peak wind events associated with small-scale circulation systems are responsible for the major part of dust deflation. For example, dust devils [Sinclair, 1973; Idso, 1974; Hess and

Spillane, 1990; Renno *et al.*, 1998] develop as dry convective vortices over the desert due to intense solar heating of the surface. This mechanism of small-scale mixing is similarly believed to be the main process of dust injection into the Martian atmosphere [Newman *et al.*, 2002; Leovy, 2003]. Dust can also be raised by the surface spreading of downdrafts in the advance of thunderstorms, incorporated within cold fronts or squall lines [Idso *et al.*, 1972]. Different parts of the globe have different names for dust uplift by this means: "haboob" in the Sudan, "harmattan"

in the Sahara, “khamsin” in Egypt, “shamal” in Iran and Iraq, and “kosa” in Japan [Idso *et al.*, 1972; Idso, 1976].

[3] Off-line tracer models attempt to represent these winds using high-resolution reanalyses: e.g., the $1.125^\circ \times 1.125^\circ$ European Centre for Medium Range Forecasts (ECMWF), the $2^\circ \times 2.5^\circ$ National Centers for Environmental Prediction and the National Center for Atmospheric Research (NCEP/NCAR), and the Goddard Earth Observing System Data Assimilation System (GEOS-DAS) reanalyses. However, tracer models cannot be used to simulate the modification of the circulation by the dust radiative heating because the analyzed winds are prescribed externally.

[4] While AGCMs allow the surface winds to respond to dust radiative heating, their generally low resolution ($4^\circ \times 5^\circ$ in the present case) is not able to produce intense, localized wind events to the same extent as the tracer models. Hence AGCMs have to parameterize wind fluctuations below the scale of the model grid box. One strategy is to tune the threshold wind speed at each grid box, so that the AGCM emission matches the value from the tracer transport model, whose surface winds are derived from one of the high-resolution reanalyses [Tegen and Miller, 1998]. Thus the threshold wind speeds are lowered in the AGCM (permitting greater emission) in regions where the reanalyses indicate greater small-scale variability in wind speed.

[5] This adjustment to account for the scale disparity between the AGCM and reanalyses has inherent difficulties. For instance, it introduces into the AGCM hundreds of “tuning knobs” associated with the horizontally varying threshold speed at each of the grid boxes that potentially emit dust. Also, the prescription of threshold wind speed builds into the AGCM errors in the tracer model distribution of dust. In order to bring the station wind observations into initial balance, the reanalyses filter out small-scale variability associated with gust fronts, dust devils, and planetary boundary layer (PBL) turbulence: circulations that raise dust. Both the NCEP and ECMWF models underestimate the observed wind strengths in certain locations [Tegen *et al.*, 2002; Mahowald *et al.*, 2002], which produce errors in dust emission given the cubic relationship between emission flux and surface wind speed. Moreover, regions of high dust emission are often remote and devoid of observations (e.g., the Sahara and Taklimakan), so that the analyzed winds are based upon information propagating within the reanalysis model from distant observing sites, thus lowering the confidence in their results. Another disadvantage is that the AGCM threshold velocities, which are tuned to represent subgrid scale variability, are fixed in time. This constraint precludes any representation of subgrid wind variability associated with the passage of a haboob, for example. Finally, the AGCM thresholds are tuned for the current climate and are generally not appropriate for different climates, such as the Last Glacial Maximum (LGM), or a warm climate forced by anthropogenic CO_2 .

[6] These limitations motivated us to restore a globally uniform threshold speed in the AGCM, but develop a method using the model meteorology to identify regions of small-scale wind variability. In fact, the AGCM already computes information about subgrid scale wind variations as part of its PBL and convective parameterizations. We follow Miller *et al.* [1992], who introduced the effect of subgrid wind fluctuations upon the surface flux of latent

heat, allowing evaporation to occur in the presence of boundary layer turbulence, even when the resolved grid box wind speed approaches zero. Lunt and Valdes [2002] adapted this technique to increase the surface flux of dust calculated by their AGCM over the Sahara and Patagonia. Here, we evaluate the effects of subgrid wind variability upon dust emission by comparison to observations. Using a slightly more elaborate parameterization of subgrid wind variability, we show that it brings our AGCM dust distribution into better agreement with the Total Ozone Mapping Spectrometer (TOMS) and advanced very high resolution radiometer (AVHRR) satellite retrievals of AOT.

[7] We identify three meteorological systems as responsible for the subgrid scale variability leading to dust emission. These are mechanical stirring within the PBL due to surface drag, dry convective thermals created by solar heating of the surface, and gust fronts created by downdrafts along the advancing edge of thunderstorms. These meteorologically preferred situations for dust emission are complementary to the preferred regions for emission identified using topographic, geomorphologic, and hydrologic criteria [Ginoux *et al.*, 2001; Tegen *et al.*, 2002; Prospero *et al.*, 2002; Zender *et al.*, 2003b; Engelstaedter *et al.*, 2003].

[8] In section 2, we review the parameterization of dust aerosols within the NASA Goddard Institute for Space Studies (GISS) AGCM. Results using a globally uniform threshold for emissions are presented in section 3 as a control experiment (hereinafter referred to as CONTROL). In section 4, we introduce a probability distribution of surface wind speed within each grid box and use the AGCM to calculate the parameters associated with this distribution. Emission now occurs even if the resolved wind speed is less than the threshold value as long as the subgrid scale variability is large enough. In section 5, we calculate emission by different mechanisms of subgrid variability, and compare the AOT corresponding to each with the TOMS and AVHRR satellite retrievals. The contributions of each mechanism are combined in section 6, where we compare total model AOT to the retrievals and CONTROL experiment. Our conclusions are given in section 7.

2. Dust Model

[9] Dust is calculated as an interactive tracer using the NASA GISS AGCM [Hansen *et al.*, 1997]. This model has horizontal resolution of 4° latitude by 5° longitude and 12 layers extending from the surface to 10 mb. The moist convection parameterization is based on a mass flux scheme developed by Del Genio *et al.* [1996]. Compared to previous parameterizations, this generates a more realistic distribution of tropical convection and moisture [Marengo and Druyan, 1994], which is important for the wet scavenging of smaller particles.

[10] The PBL is simulated using a second-order turbulence model [Hartke and Rind, 1997; Mellor and Yamada, 1982; Canuto *et al.*, 1994; Cheng *et al.*, 2002], applied to a secondary grid of eight levels nested between the surface and the middle of the first AGCM layer, a depth of roughly 200 m. Mixing across this grid is driven by shear and buoyancy sources; static instabilities over a deeper layer are eliminated by a separate dry convection parameterization, which mixes tracers and momentum, while homogenizing

potential temperature within the column. Similarity theory is used to relate the winds at the base of the PBL to the surface. Compared to an Ekman parameterization [Hansen *et al.*, 1983], the second-order closure scheme results in a stronger tropical surface circulation [Marengo and Druyan, 1994]. Tracers (including dust) are advected using the quadratic upstream scheme [Prather, 1986], which computes the slope and curvature of a variable in addition to its grid box average, thus increasing the effective resolution of the dust compared to the actual grid resolution.

[11] The spatial distribution of mineral dust is determined by the competition of three mechanisms that interact every model time step: emission, transport, and deposition. Because these processes are size-dependent, it is natural to divide mineral dust into independent size classes. We choose four classes as a balance between detailed description and computational efficiency: one for clay (with particle radii between 0.1 and 1 μm) and three for silt (1–2 μm , 2–4 μm and 4–8 μm). Particles larger than 8 μm are responsible for 1% of the dust radiative forcing [Tegen *et al.*, 1996] and are neglected. Particles with radii less than 1 μm are transported as one class because they are not fractionated by gravitational settling due to the particles' similar fall speeds. However, in the radiative transfer calculations, the smallest size class is further divided into four bins, with an effective radius of 0.1, 0.2, 0.4, and 0.8 μm , respectively [Tegen *et al.*, 1996].

[12] Wind tunnel studies [Gillette, 1978] show that dust deflation is proportional to the third power of the surface friction speed w_* (equal to $\sqrt{\tau/\rho}$ where τ is the surface wind stress and ρ is the air density). The friction speed is related to the surface wind speed w through the roughness length z_0 [Stull, 1988]. In the absence of a global data set for z_0 , we idealize it as a constant [Zender *et al.*, 2003a]. Then we can reformulate emission in terms of the surface wind speed:

$$Q = \begin{cases} CF(r)(w - w_t)w^2 & \text{for } w \geq w_t \\ 0 & \text{for } w < w_t \end{cases} \quad (1)$$

where Q is the dust emission, w is the surface wind speed at 10 m, and w_t is the threshold wind speed. Although equation (1) relates wind speed to emission of silt and clay particles, this is accomplished indirectly by saltation bombardment (sandblasting) of larger sand particles onto silt and clay dust grains [Bagnold, 1941; Iversen and White, 1982; Gomes *et al.*, 1990; Shao *et al.*, 1993, 1996; Alfaro *et al.*, 1997; Lu and Shao, 1999]. The kinetic energy of the saltating sand particles breaks the cohesive bonding of the smaller particles and helps mobilize them at much lower wind speeds than would be required to overcome directly the cohesive forces. We assume w_t represents the threshold for the saltating particles that are first lifted by the wind. These in turn liberate from the surface the smaller particles that we explicitly model. The factor C is a dimensional constant ($\mu\text{g s}^2 \text{m}^{-5}$) assumed to be the same for all size classes. The factor $F(r)$ is the fractional areal coverage of clay or silt within the grid box, which is estimated from the $1^\circ \times 1^\circ$ soil type and particle size data sets of Zobler [1986] and Webb *et al.* [1991]. Potential source areas are identified using the vegetation data set of Matthews [1983]. Dust is emitted over the arid and semiarid regions, as well as from

soils disturbed by overgrazing, deforestation, cultivation, and the shift in the Saharan/Sahelian boundary [Middleton and Thomas, 1992; Hammond, 1992; Tucker *et al.*, 1991; Tegen *et al.*, 1997]. In addition to these constraints, emission requires the soil moisture to be low. In order to satisfy this condition, evaporation must exceed precipitation in each grid box for a certain duration which depends on the soil texture. For coarse texture (sand), medium texture (silt), and fine texture (clay), the soil desiccation times are 20, 50, and 150 hours, respectively [Tegen and Miller, 1998]. These different timescales take into account the different moisture diffusivity of soil types [Gardner, 1983]. There is no emission over snow or ice covered surfaces. Finally, the model assumes an unlimited availability of the soil particles for emission, ignoring any possible surface crusting effects.

[13] The soil data sets used to calculate particle availability are constructed for agricultural purposes, and may not be the most accurate survey of particles susceptible to erosion. Recently, Prospero *et al.* [2002] provided evidence using the TOMS aerosol index satellite retrieval that former lake beds provide an abundance of small clay-sized particles that are loosely bound, thus dominating dust emission. Certain studies use the location of former lake beds to identify “preferred” sources of erodible particles, either as an alternative or in addition to soil particle availability inferred from agricultural maps [Ginoux *et al.*, 2001; Tegen *et al.*, 2002; Mahowald *et al.*, 2002; Zender *et al.*, 2003a]. At present, we do not include “preferred” sources, even though they lead to improved dust aerosol distributions in the above studies.

[14] Once the dust particles are emitted from the surface, they scatter sunlight and terrestrial radiation and get transported by the winds. Dust radiative forcing is calculated as described by Tegen and Lacis [1996] and Miller *et al.* [2004]. All of our experiments allow dust radiative forcing to modify the circulation, a feedback prohibited in tracer models, where the circulation is prescribed [Guelle *et al.*, 2000; Ginoux *et al.*, 2001; Mahowald *et al.*, 2002]. Perlwitz *et al.* [2001] show that dust radiative forcing reduces the aerosol burden by about 15%, although without altering the geographic distribution. Therefore we expect the geographic distribution of emission to be similar whether or not dust radiative forcing is included.

[15] The particles eventually return to the surface either by dry or wet deposition. Dry deposition has two modes: turbulent mixing of dust particles in the first model layer and gravitational settling throughout the column [Tegen and Fung, 1994]. This is an efficient process for large silt particles. Wet deposition depends on the AGCM surface precipitation and scrubs the column according to the cloud height calculated by the model, which is in contrast to the specified height used by Miller and Tegen [1998]. This process is the main removal mechanism for smaller, far-traveled dust particles, due to their small Stokes velocities. There is no remobilization of settled dust.

3. CONTROL Experiment Without Subgrid Variability

3.1. Methodology

[16] To calculate the effect of subgrid variations in wind speed, we compare the AGCM dust distribution to a

Table 1. Table of Experiments Together With the Ratio of the Emission Factor C in Equation (1) Scaled by C for the CONTROL Experiment

Experiment Name	Description	$\frac{C}{C_{\text{CONTROL}}}$
CONTROL	$w_t = 4^a$	1.0
TKE	$\sigma \propto w_p$	0.7
DRY	$\sigma \propto w_d$	0.4
MOIST	$\sigma \propto w_m$	1.0
ALLSUBGRID	$\sigma \propto w_p + w_d + w_m$	1.2
SENSITIVITY 1	$\sigma \propto \sqrt{w_p^2 + w_d^2 + w_m^2}$	3.3
SENSITIVITY 2	$\sigma \propto w_d + w_m$	4.0
SENSITIVITY 3	$\bar{w} + w_p + w_d + w_m$	3.8

^aValue is in ms^{-1} .

simulation where these variations are absent. In all experiments, we hold the global, annual dust emission constant. This way, the differences between the experiments will portray contrasts in the geographic distribution of mineral dust and not changes in the total emission. To impose an identical global emission upon each experiment, we adjust the coefficient C relating emission to wind speed (compare equation (1)). It is important to realize that C is not a universal parameter; it depends upon model resolution and the precise formulation of emission (e.g., whether emission is proportional to the third or fourth power of wind speed). Modelers routinely tune C to match observations of dust optical thickness, surface concentration, and deposition. In contrast to C , the global emission is independent of the model, having a single value for a given particle size range that is potentially measurable, albeit poorly known at present.

[17] A global, annual emission target of 2000 Tg yr^{-1} is employed. This is in the range of current model [Mahowald *et al.*, 1999, 2003; Zender *et al.*, 2003b] and observational estimates [Duce, 1995]. In practice, it is time consuming to impose the same global emission upon each model, due to nonlinear feedbacks by dust radiative forcing upon dust emission, and we will tolerate departures from our target by up to 5%. This departure is small compared to the sensitivity of the geographic variations in dust that we calculate. Table 1 shows the different experiments that are performed in this paper and their corresponding ratios of C with respect to that of the CONTROL experiment. By holding global emission constant, the factors we identify as controlling the geographic distribution of dust will be robust even if the actual observed emission is later found to depart substantially from our assumed value of 2000 Tg yr^{-1} . In this event, we would simply adjust C to achieve the correct emission. Conceptually, our normalization approach is analogous to the experiments of Reader *et al.* [1999] who computed the dust distribution from a unit source strength. As alternative to emission, we could of course keep the total load fixed, but we somewhat arbitrarily choose to fix global emission.

[18] The model is integrated with climatological sea surface temperatures (SST) for six model years and the last five years are used to evaluate the model results. This integration time is long enough to give robust, statistically significant, differences between experiments but short enough to be computationally efficient. Prescribed SST experiments lack decadal modes of variability which are usually associated with the variations in the SST [Miller and

Del Genio, 1994], hence making the model interannual variability smaller and statistical significance larger.

3.2. CONTROL Experiment

[19] As a control experiment, emission is calculated using equation (1) with the surface wind speed w given by the value explicitly calculated by the AGCM at each grid box. (Subgrid wind variability will be introduced in the next section.) The wind speed threshold for emission w_t is set equal to the globally uniform value of 4 ms^{-1} , in contrast to the geographically varying value used by Tegen and Miller [1998]. In reality, the threshold wind speed varies with surface roughness [Marticorena and Bergametti, 1995], although in the absence of global roughness observations we overlook this variation in the present study.

[20] Our experiments are compared to the TOMS AOT [Herman *et al.*, 1997; Torres *et al.*, 2002], over both land and ocean, and to AVHRR AOT [Husar *et al.*, 1997], only over the ocean. The satellite retrievals in this study represent climatologies for the period 1984–1989. In contrast, our SST is prescribed from a 1951–1980 average. A more appropriate comparison would have been based upon same observing period for the retrievals and SST. In addition to offering an independent data set with which to evaluate dust models, satellite retrievals allow comparisons over larger regions, which reduces the importance of transport errors in the AGCM. Thus satellite retrievals might be more definitive test of dust emission in an AGCM than observations at a single location. Nevertheless, a comparison to Aerosol Robotic Network (AERONET) has been done by Cakmur [2003]. The CONTROL experiment generally compares poorly downwind of major dust source regions, although it is hard to know whether this reflects deficiencies in the aerosol model, or else biases in the AGCM winds or rainfall.

[21] Figure 1 shows the model and retrieved AOT in eight regions where the dust load is expected to be large and dominate the retrieval: AVHRR is the white line bounded by light shading and TOMS is the white line bounded by dark shading. The shading indicates one standard deviation above and below the mean. The standard deviation measures the magnitude of time variations, and does not include uncertainty due to retrieval error. At ocean sites, where both retrievals are available, we observe similarities in the phase between the two data sets, but find that the TOMS amplitude invariably exceeds that of AVHRR. Myhre *et al.* [2004] find that this offset is generally present over oceanic regions.

[22] This offset may be due to a couple of reasons. For example, the optical thickness is retrieved by the two satellites at different wavelengths: 630 nm and 380 nm for AVHRR and TOMS, respectively (in comparison to the 550 nm AOT computed by the AGCM). The difference between the AOT within this range of wavelength is small for large dust particles (of order microns), and large for small particles like soot. Since we are considering regions where dust is the predominant aerosol, we assume that there are negligible differences between optical thickness at these two wavelengths, although in regions of far-traveled dust where the particles are small, the 380 nm TOMS AOT will correspond to a larger value than that measured at the 630 nm AVHRR wavelength. On the basis of POLDER

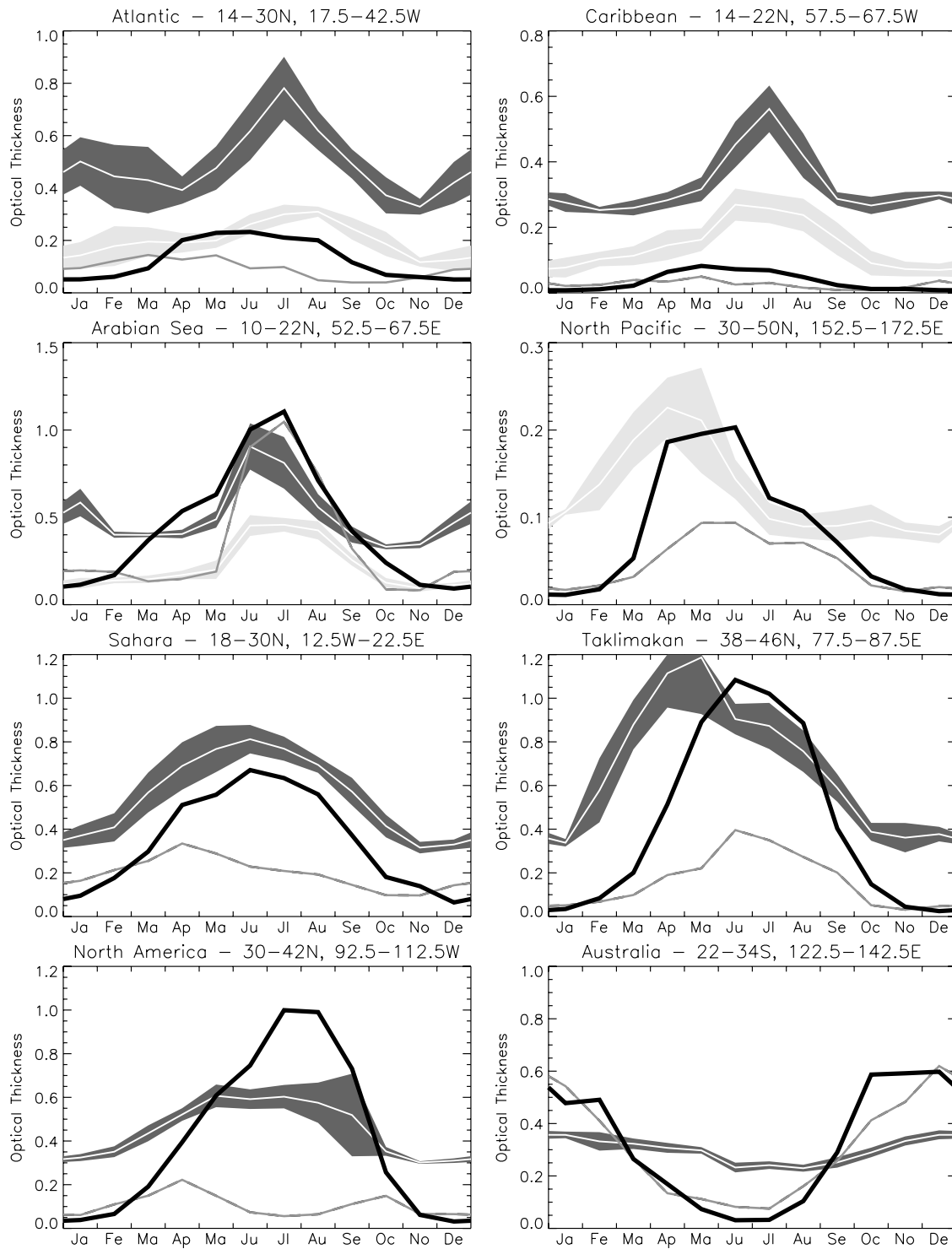


Figure 1. Regional averages of optical thickness. The thick solid black line is the ALLSUBGRID experiment, the solid gray line is the CONTROL experiment, the white line flanked by dark shading is the TOMS retrieval, and the white line bounded by light shading is the advanced very high resolution radiometer (AVHRR). The shading about the retrievals indicates one standard deviation above and below the mean, a measure of variability with respect to time and not measurement uncertainty. The AVHRR retrieval is available only over ocean. The TOMS retrieval is not shown over the North Pacific due to persistent cloud cover.

retrievals of the Angstrom exponent [Chiapello *et al.*, 2000], we estimate that the difference between the 380 and 630 nm AOT's is of order 20% or less.

[23] Also, the TOMS retrieval of AOT assumes an aerosol layer height derived from the tracer model of Ginoux *et al.* [2001], which is used to convert the TOMS radiances into an AOT. To the extent that the tracer model underestimates the actual aerosol layer height, the TOMS AOT will overestimate the actual AOT value. In the absence of detailed observations of the vertical distribution of dust, it is difficult to quantify this uncertainty of the TOMS AOT and its difference with respect to the AVHRR retrieval. Imprecise cloud screening may also cause the TOMS retrieval to overestimate the AOT by as much as 0.1. Evaluation of the model AOT is complicated by contamination of the retrieval by other aerosols (black carbon in the case of TOMS; sulfates, organics and sea salt in the case of AVHRR). However, as noted above, the analyzed regions were chosen for their dominant contribution of dust to the total aerosol burden. Given the uncertainties in deriving both TOMS and AVHRR AOT, we desire that the AGCM results lie somewhere between the two retrievals.

[24] The seasonal cycle of AOT calculated by the CONTROL experiment is shown in Figure 1. The left column of Figure 2 shows the spatial pattern of the optical thickness for the CONTROL experiment. Compared to the satellite retrievals, the dust optical thickness is underestimated over the subtropical Atlantic Ocean. Also, there is a lack of dust loading over the Sahara during most of the seasons. The model underestimates emission over the Taklimakan source region, and thus underestimates the dust optical thickness over central Asia, and downwind over the North Pacific. In addition, the North American dust load is low in the model, although other aerosol types may contribute to the retrieval at this location. On the other hand, the model overestimates the source region over Australia during the Southern Hemisphere summer. These are the aspects of the model that we strive to improve.

[25] We evaluate the AGCM representation of the Saharan Aerosol Layer (SAL), within which dust is transported across the Atlantic [Carlson and Prospero, 1972]. Dry convection is observed to mix the dust 3–5 km above the surface of the North African deserts, where it can be transported long distances downwind by the midlevel African Easterly jet [Karyampudi *et al.*, 1999]. As the dust layer exits the African continent between 10°–25°N during Northern Hemisphere summer, it is undercut by cool and moist monsoonal air. The SAL is a well-mixed layer, confined above 1–2 km, but below its neutral buoyancy level near 5 km, like an air duct [Karyampudi *et al.*, 1999]. In order to diagnose the model SAL over the tropical Atlantic Ocean, three intersecting transects of the model dust mixing ratio are computed: one near the African coast at 22.5°W longitude (Figure 3, left column), and the other at 14° and 18°N latitude (Figures 4a and 4b). As indicated by Figure 3 (left column), the AGCM plume shifts its central latitude according to the movement of ITCZ. In the winter, the model plume is located around 15°N, 5°–10° too far north according to satellite retrievals [Husar *et al.*, 1997; Herman *et al.*, 1997], although the discrepancy could be due to aerosol loading by biomass burning south of 15°N, included in the retrievals [Tegen and Fung, 1994; Takemura

et al., 2000]. As Northern Hemisphere summer approaches, the model plume location shifts northward to 20°N, consistent with the retrievals. Both the summer and autumn loading are much lower in the model compared to spring and winter. Closer to the equator, the dust mixing ratio falls toward zero because of the heavy precipitation associated with the ITCZ.

[26] Figures 4a and 4b show the westward extension of the plume during the summer season, when there is heavy dust loading over the Sahara. In contrast to observations [Karyampudi *et al.*, 1999], the AGCM SAL does not extend much beyond the coast of Africa which leads to low optical depths over the Atlantic Ocean, as shown in Figure 2. By incorporating the effects of subgrid scale variability into the dust model, we will show that a more realistic representation of dust emission is achieved, along with a better representation of the SAL.

4. Development of the Wind Speed Distribution

[27] In the CONTROL experiment, the surface wind speed w is represented by the wind speed explicitly calculated by the AGCM at each grid box. In order to incorporate variability due to subgrid scale circulations, we introduce a probability distribution of wind speed within each grid box, as shown in Figure 5 (right). Therefore emission is computed according to the fraction of the probability density function (PDF) that exceeds the threshold value (denoted by the shaded area in Figure 5):

$$Q = CF(r) \int_{w_t}^{\infty} w^2 (w - w_t) p(w) dw, \quad (2)$$

where $p(w)$ is the distribution of wind speed w within the grid box, and w_t is the threshold speed.

[28] To derive the wind speed PDF, we assume that the zonal (u) and the meridional (v) components of the wind velocity can be represented by a bivariate normal distribution as shown in Figure 5 (left):

$$n(u, v) du dv = \frac{1}{2\pi\sigma_u\sigma_v\sqrt{1-\rho^2}} \cdot \exp \left[-\frac{\left(\frac{u-\bar{u}}{\sigma_u}\right)^2 - 2\rho\left(\frac{u-\bar{u}}{\sigma_u}\right)\left(\frac{v-\bar{v}}{\sigma_v}\right) + \left(\frac{v-\bar{v}}{\sigma_v}\right)^2}{2(1-\rho^2)} \right] du dv, \quad (3)$$

where \bar{u} and \bar{v} are the zonal and meridional components of velocity, respectively, calculated explicitly by the AGCM at each grid box; σ_u and σ_v are the standard deviation of subgrid fluctuations in either direction [Freund and Walpole, 1987]. The variable ρ is the correlation coefficient between the components of the horizontal fluctuations:

$$\rho = \text{cor}(u, v) = \frac{\sigma_{uv}}{\sigma_u\sigma_v}. \quad (4)$$

We assume ρ is zero, given that there is no evidence showing fluctuations in u or v to be generally related to each other [Caughey and Palmer, 1979]. To simplify the bivariate normal distribution further, we make a second

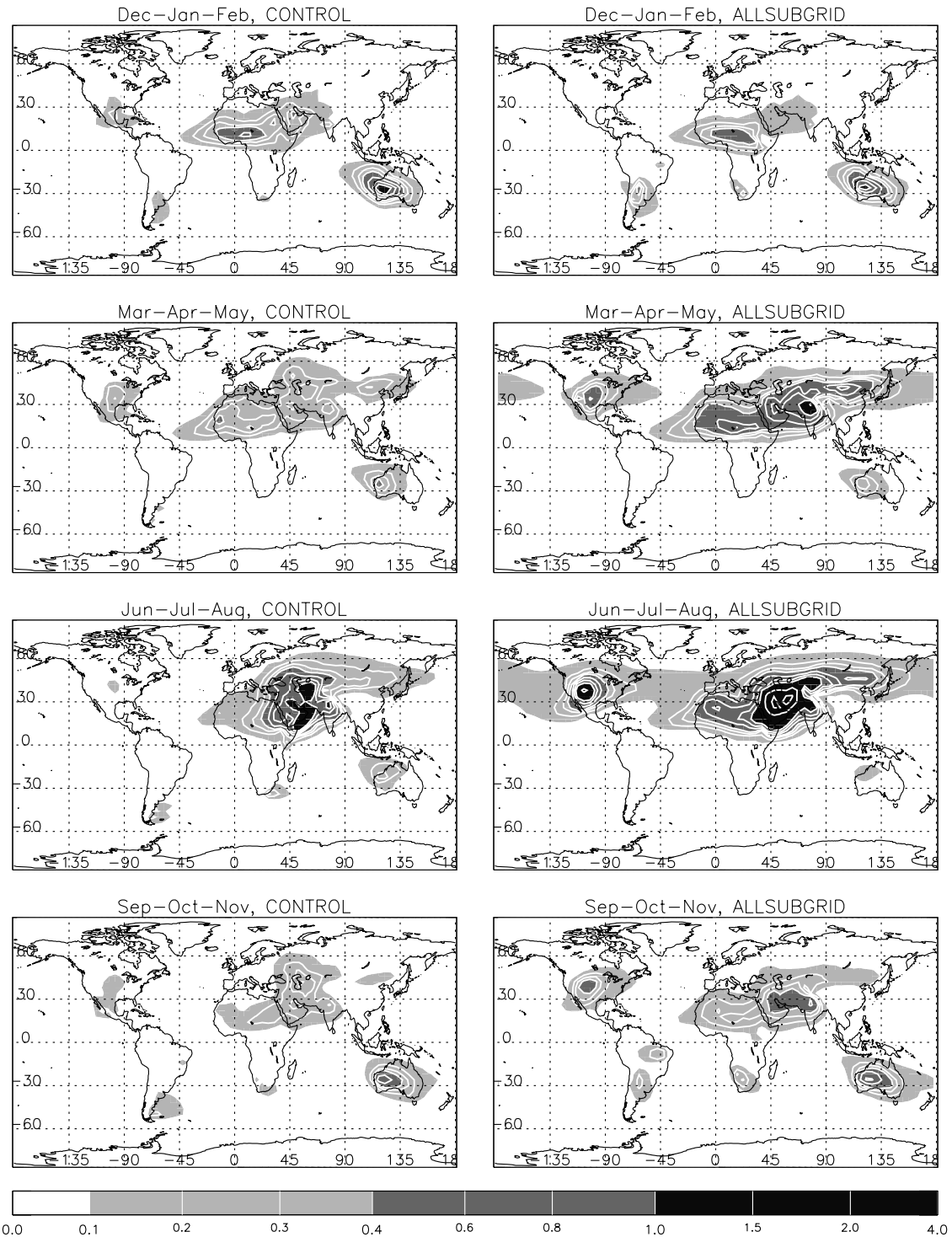


Figure 2. Seasonal average of optical thickness for the (left) CONTROL and (right) ALLSUBGRID experiments.

assumption that σ_u equals σ_v , representing both as σ . In accordance with our assumption of isotropy, the observational study by *Panofsky et al.* [1977] indicates that fluctuations in both horizontal components may be approximated by the same formula within convective conditions. In order to derive a distribution of wind speed (as opposed to velocity), we perform a transformation of variables, $u = w \cos \theta$, $v = w \sin \theta$, and thereafter we

compute the PDF as a function of the wind speed w and direction θ . Now, rewriting equation (3) in terms of w and θ gives us (defining $\bar{u} \equiv \bar{w} \cos \bar{\theta}$, $\bar{v} \equiv \bar{w} \sin \bar{\theta}$)

$$n(w, \theta) dw d\theta = \frac{w}{2\pi\sigma^2} \exp\left[-\frac{1}{2\sigma^2}(w^2 + \bar{w}^2)\right] \cdot \exp\left[\frac{w\bar{w}}{\sigma^2} \cos(\theta - \bar{\theta})\right] dw d\theta. \quad (5)$$

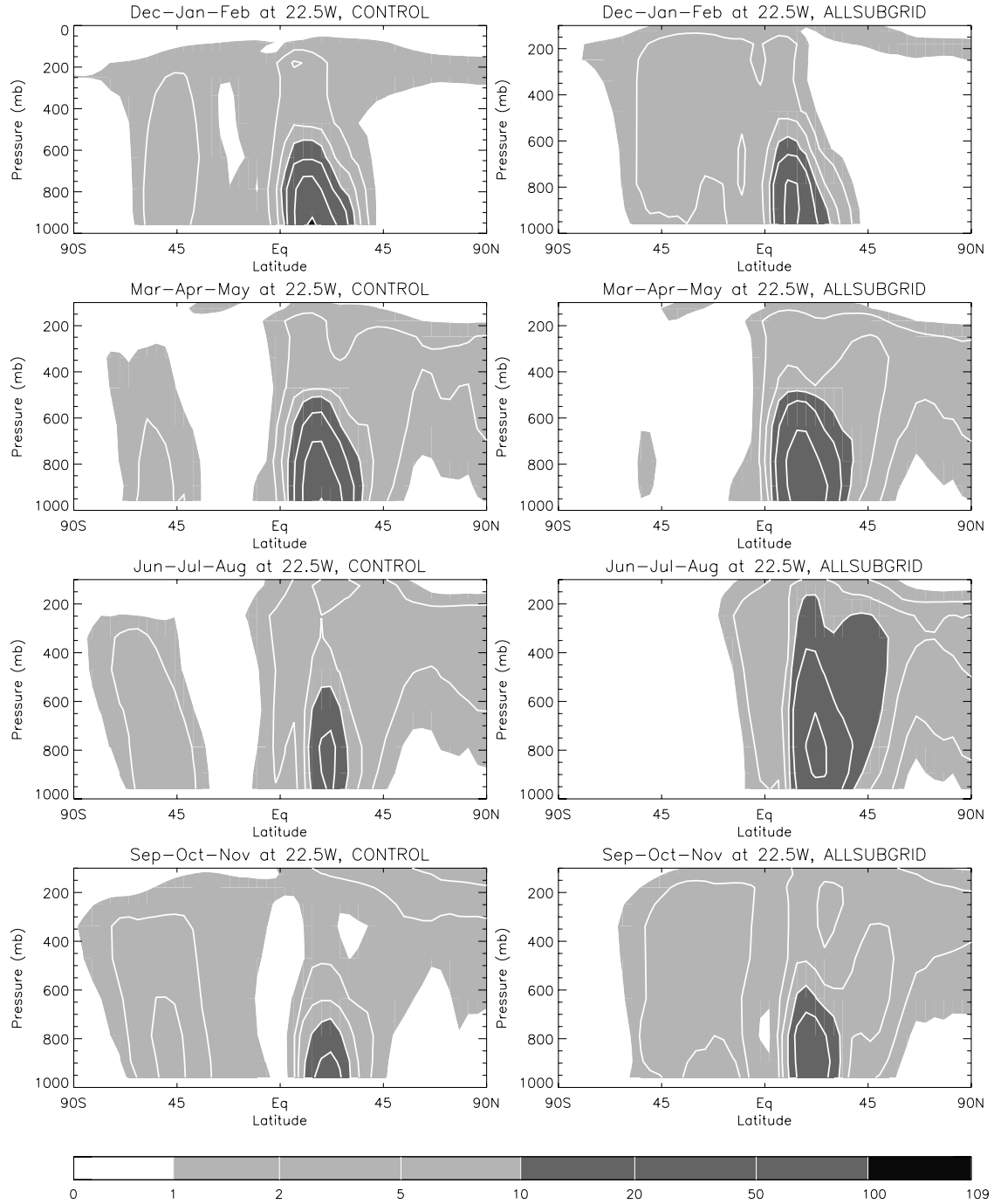


Figure 3. Dust mixing ratio ($\mu\text{g kg}^{-1}$) at 22.5°W for both the (left) CONTROL and (right) ALLSUBGRID experiments.

To derive a wind speed distribution $p(w)$, we integrate over all directions θ , obtaining the following PDF for the wind speed w [Abramowitz and Stegun, 1985]:

$$p(w)dw = I_0\left(\frac{w\bar{w}}{\sigma^2}\right) \frac{w}{\sigma^2} \exp\left[-\frac{1}{2\sigma^2}(w^2 + \bar{w}^2)\right] dw, \quad (6)$$

where I_0 is the modified Bessel function of order zero, which is conveniently integrated numerically [Press et al., 1996].

[29] As the resolved speed approaches zero, this equation approaches the familiar Rayleigh distribution, used to parameterize dust emission by Westphal et al. [1988]. The Rayleigh distribution is a special case of the Weibull family of distributions, where the shape parameter is 2. Many studies of electricity generation by wind propose the Weibull distribution as an empirical representation of the distribution of wind speed [Justus and Mikhail, 1976; Carlin and Haslett, 1982; Conradsen et al., 1984; Christofferson, 1987; Pavia and O'Brien, 1986]. These measurements motivated the adoption of this distribution

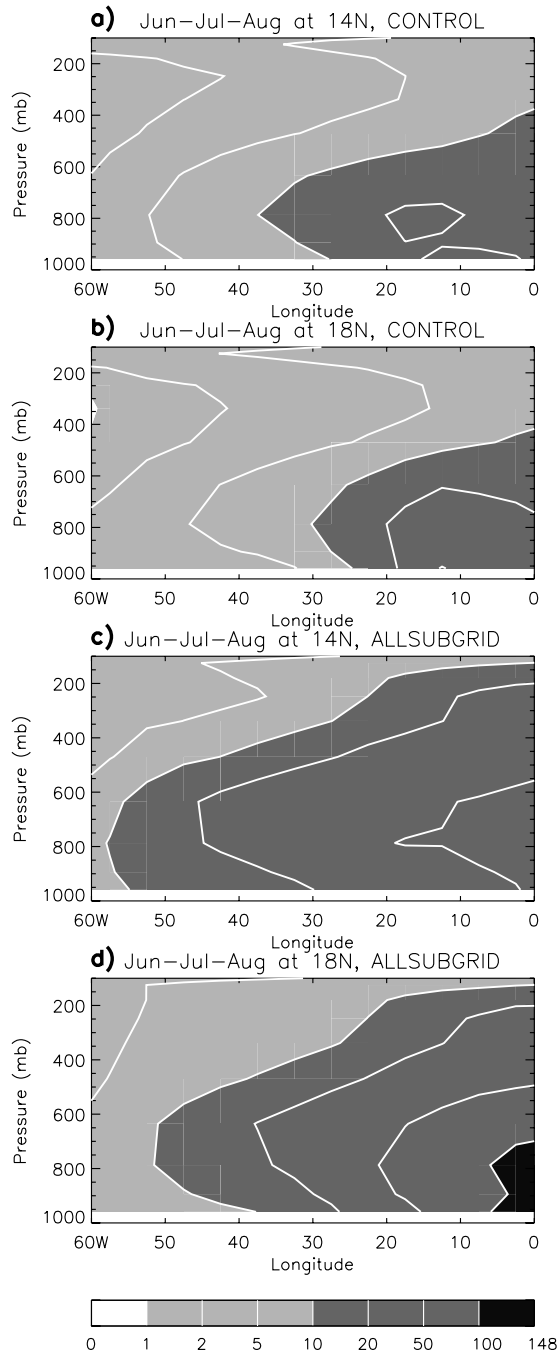


Figure 4. Dust mixing ratio ($\mu\text{g kg}^{-1}$) at (a, c) 14°N and (b, d) 18°N for both the CONTROL and ALLSUBGRID experiments. The west coast of Africa is around 20°W .

by Gillette and Passi [1988] to compute dust emission. The correspondence between empirical distributions of wind speed and our distribution of equation (6) is welcome given our somewhat arbitrary choice of a normal distribution for the individual components of the surface velocity. To be sure, there are few observations of wind with high time resolution over a wide range of surface types to guide us. Our choice of a normal distribution in equation (3) neglects higher-order moment parameters such as skew and kurtosis. The only parameter that must be supplied beyond

the speed of the wind explicitly calculated by the AGCM is the variance of the fluctuations. This simplicity motivates our assumption of normality in the absence of observations to the contrary. Conversely, it gives credence to the use of a Weibull distribution as an empirical fit, given that it can be derived as a consequence of such a generic distribution as equation (3).

[30] We show in Figure 6a that due to subgrid wind variability, the mean wind speed, $\int_0^\infty wp(w)dw$, always exceeds the explicitly resolved speed \bar{w} . As in the work of Miller *et al.* [1992] and Lunt and Valdes [2002], the mean speed remains nonzero, given subgrid variability, even if the AGCM resolved wind slackens to zero. Note that both the speed of the mean wind velocity (e.g., the magnitude of resolved wind, \bar{w}) and the standard deviation of velocity distribution (σ) shown on the left side of Figure 5 are distinct from the mean and the standard deviation of the wind speed distribution (\bar{w}_s and σ_s), shown on the right side of Figure 5.

[31] Finally, in order to compute the dust flux Q , we include $p(w)$ in the modified dust emission formula (2):

$$Q(\bar{w}, w_t, \sigma) = CF(r) \int_{w_t}^{\infty} \frac{w^3 (w - w_t)}{\sigma^2} I_0\left(\frac{w\bar{w}}{\sigma^2}\right) \cdot \exp\left[-\frac{1}{2\sigma^2} (w^2 + \bar{w}^2)\right] dw. \quad (7)$$

Figure 6b shows the behavior of the emission equation (7) for $w_t = 8 \text{ ms}^{-1}$. In the absence of subgrid wind variations, there is emission only when \bar{w} exceeds the threshold speed, as in the CONTROL experiment. However, if subgrid variability exists, emission can occur even if the resolved wind speed \bar{w} is below the threshold. The speed \bar{w} is computed explicitly by the AGCM at each grid box. What remains is to calculate σ , the scale of horizontal velocity fluctuations, using the PBL and convective parameterizations.

5. Velocity Scales for Subgrid Variability

[32] We represent three meteorological mechanisms responsible for the subgrid scale variability leading to dust emission. These are mechanical mixing within the PBL due to surface drag, dry convective thermals, and gust fronts created by moist convective downdrafts. The subgrid velocity fluctuations represented by the AGCM PBL parameterization are confined to within 200 m of the surface. Thus the PBL parameterization does not represent the entire spectrum of surface variability due to dry and moist convection, nor their contribution to the wind fluctuations characterized by σ . Instead, we calculate σ associated with deeper eddies using the dry and moist convective parameterizations within the AGCM. In our initial experiments, we set the wind speed threshold to the globally uniform value of 4 ms^{-1} and compute dust emission by each parameterization separately.

5.1. PBL Velocity Scale

[33] Because the wind vanishes right at the surface, the shear produced by the decrease in the wind speed within the boundary layer causes turbulent mixing. Convective thermals driven by surface heating can also contribute to TKE if

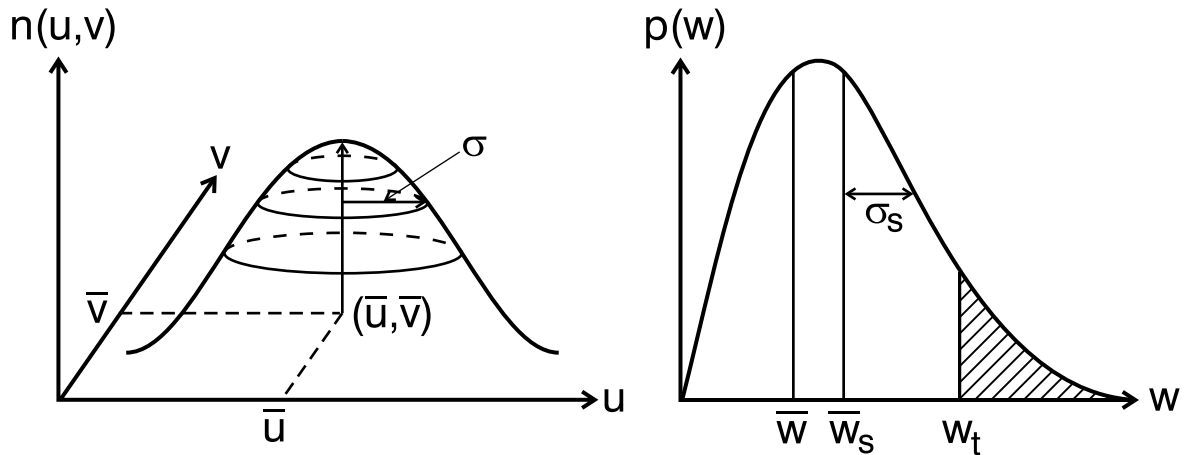


Figure 5. Probability functions representing the distribution of (left) wind velocity and (right) wind speed within the model grid box. Note that the mean wind speed $\bar{w}_s \equiv \int_0^\infty wp(w)dw$ is distinct from the speed of the mean wind $\bar{w} \equiv \sqrt{\bar{u}^2 + \bar{v}^2}$ that is explicitly calculated by the atmospheric general circulation model (AGCM). Similarly, the standard deviation of the wind speed, $\sigma_s \equiv \int_0^\infty (w - \bar{w}_s)^2 p(w)dw$, differs from σ , the standard deviation of each component of the wind velocity.

their vertical extent remains within the 200 m depth of the model's PBL. Given our assumption of isotropy, the turbulent kinetic energy is partitioned equally in all three dimensions. The standard deviation σ in equation (6) is taken to be the square root of two thirds of the TKE, which is provided by the model's PBL parameterization. The spatial distributions of TKE and surface wind speed (not shown) resemble each other: in regions of high TKE, interior momentum is mixed down efficiently to the surface. Figure 7 (top) shows the Northern Hemisphere summer average diurnal cycle of the TKE velocity scale over the Sahara and the frequency distribution of this scale computed over the whole globe. As expected, the velocity scale rises in the morning hours as the Sun's radiation stirs up the boundary layer. It reaches a maximum value of about 0.5 ms^{-1} at noon then decays slowly back to its original value of 0.3 ms^{-1} . The global frequency spectrum shows that the most intense gusts are the rarest.

[34] The seasonal variation of dust emission, Q , due to PBL fluctuations is shown in Figure 8 as a dotted line. (This experiment is hereafter referred to as the TKE model). The close similarity between the CONTROL (solid gray) and the TKE experiment illustrates that TKE computed by the GISS PBL parameterization contributes little to dust emission, beyond that raised by AGCM's explicitly calculated surface winds.

5.2. Dry Convective Velocity Scale

[35] Next we represent the variability due to dry convection by assigning it a characteristic velocity scale. Dry convection is associated with solar heating of the surface especially during the summer, and mixes dust from the surface layer to the free troposphere [Schulz *et al.*, 1998]. Convective activity is characterized by deep isentropic mixing that over West Africa extends up to 5–6 km in height [Karyampudi *et al.*, 1999; Karyampudi and Carlson, 1988; Westphal *et al.*, 1988]. In fact, it is crucial that the dust layer extends to high levels in order to avoid rain out by cumulus clouds below the Atlantic trade wind inversion and travel to the Caribbean, some 6000 km away. In the

CONTROL experiment, dry convection is incapable of raising dust from the surface, only mixing it vertically within the column.

[36] Dry, convective plumes are a nonlinear system that exhibit fully turbulent conditions. Despite the lack of detailed knowledge of the circulation within the plume, observations show consistent and repeatable gross characteristics that make it possible to infer an empirical relationship for the velocity scale. The relevant quantities for deriving a dry convective velocity scale in the mixed layer include the boundary layer height H , the buoyancy factor g/T and the kinematic heat flux $(Q_h/\rho c_p)$, where g is the gravitational constant, T is the surface temperature, Q_h is the surface heat flux, ρ is the density of air, and c_p is the specific heat at constant pressure [Arya, 1988].

[37] Following Miller *et al.* [1992] and Lunt and Valdes [2002], we compute a velocity scale for dry convection w_d , using

$$w_d = \begin{cases} \left(\frac{Q_h g H}{\rho c_p T} \right)^{\frac{1}{3}} & \text{when dry convection is present} \\ 0 & \text{otherwise} \end{cases} \quad (8)$$

This equation accounts for emission by dry convective eddies that extend above the first AGCM layer, beyond the domain of the AGCM's PBL parameterization. The convective velocity scale characterizes the vertical velocity induced by the production of turbulence due to buoyancy. Q_h is approximated as the surface sensible heat flux as by Renno *et al.* [1998].

[38] There is the evidence from computations [Deardorff, 1974], laboratory experiments [Willis and Deardorff, 1974], and atmospheric data from Kansas (J. C. Wyngaard and Y. Izumi, unpublished data, 1971), showing that when dry convection is present, equation (8) is representative of the horizontal velocity fluctuations at the surface [Wyngaard and Cote, 1974; Wyngaard, 1985]. Observations at Cardington, UK and Fort Eglin, Florida, USA also show similar ranges for both horizontal and vertical velocity fluctuations under unstable conditions [Caughey and Readings, 1975].

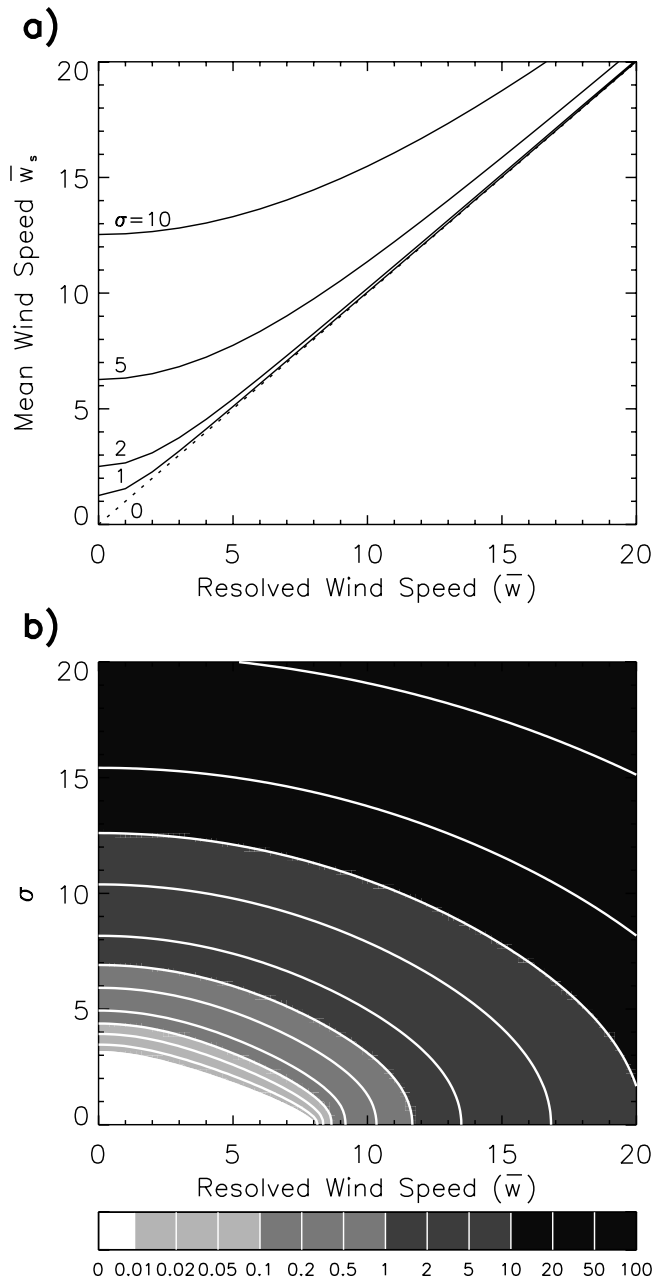


Figure 6. (a) Mean wind speed $\bar{w}_s \equiv \int_0^\infty wp(w)dw$ as a function of the subgrid variability. Each line represents a different value of σ , the scale of subgrid fluctuations (compare equation (3)). The dotted line corresponds to $\sigma = 0$, i.e., the case of zero subgrid variability. (b) Quantity $\int_{w_i}^{\infty} w^2(w - w_i)p(w)dw$, proportional to emission, as a function of σ and the mean wind speed \bar{w} . Darker shading corresponds to greater emission.

Moreover, the thermodynamic theory derived by Renno *et al.* [1998] argues that horizontal and vertical velocities due to convection are of the same order of magnitude.

[39] Convective velocity scales calculated according to equation (8) show good agreement with values measured during field experiments in Wangara, Australia [Stull, 1988] and elsewhere [Lenschow and Stephens, 1980; Hess and Spillane, 1990]. Figure 7 (middle) shows the average

diurnal cycle of the dry convective velocity computed by our model over the Northern Hemisphere summer Sahara. The maximum peaks a couple of hours past the local noon and has an approximate value of 1.5 ms^{-1} , in accordance with the literature mentioned above. The frequency spectrum shows peaks around $1\text{--}3 \text{ ms}^{-1}$ with decreasing frequency as the speed increases.

[40] The seasonal plot of emission when the dry convective velocity scale is implemented in the model is shown in Figure 8 as the thick solid black line; this experiment is hereafter referred to as the DRY model. The inclusion of dry convection as a source of subgrid wind fluctuations emphasizes locations that are recognized as major dust emitters. In the DRY experiment, emission is favored over regions such as the Saharan and Taklimakan deserts. The latter region is regarded as one of the largest dust exporting deserts over the North Pacific. In Central Asia, emission shifts during the summer from the Caspian Sea area toward the Thar and Rajasthan deserts, more in agreement with the TOMS and Meteosat retrievals (not shown) compared to the CONTROL experiment [Herman *et al.*, 1997; Léon and Legrand, 2003].

5.3. Moist Convective Velocity Scale

[41] Dust raised by moist convection is linked to the strength of the downdraft within a Cumulonimbus cloud. These clouds are often related to the arrival of a cold front or thunderstorms on the advancing edge of a squall line [Idso *et al.*, 1972]. The dust storms that form over the deserts during deep convective activity are called haboobs, the Arabic word for violent wind. When the Cumulonimbus cloud reaches its mature stage, the frictional drag exerted by the falling rain and the negative buoyancy due to the evaporating droplets produce a cold downdraft. The air associated with the downdraft typically originates at levels of 900–600 mb [Houze and Betts, 1981; Del Genio and Yao, 1988, 1993]. In severe cases, these downdrafts can spread horizontally in advance of the storm by more than 150 km and reach peak gusts of 45 ms^{-1} : a hurricane strength wind [Lawson, 1971; Morales, 1986; Ahrens, 1994]. This horizontal current of cold air can produce a wall of dust as tall as 4 km [Idso, 1976].

[42] Our parameterization derives the moist convective velocity scale in proportion to the downdraft mass flux, following [Emanuel and Rothman, 1999]

$$w_m = \frac{\beta M_d}{\rho \sigma_m}, \quad (9)$$

where β is an empirical constant typically set equal to 10 [Emanuel and Rothman, 1999], ρ is the air density, σ_m is the fractional area of the grid box (0.05) where the downdraft occurs, and M_d is the downdraft mass flux that the model computes. In the GISS model, the downdraft mass flux is specified to be one third of the updraft mass flux [Del Genio and Yao, 1993], consistent with the observation that updrafts are stronger than downdrafts. Similar to the dry convective parameterization, moist convection in the CONTROL experiment mixes dust vertically without altering the surface wind speed.

[43] Again, we assume isotropy and equate the horizontal and vertical velocity scales. We allow emission by moist

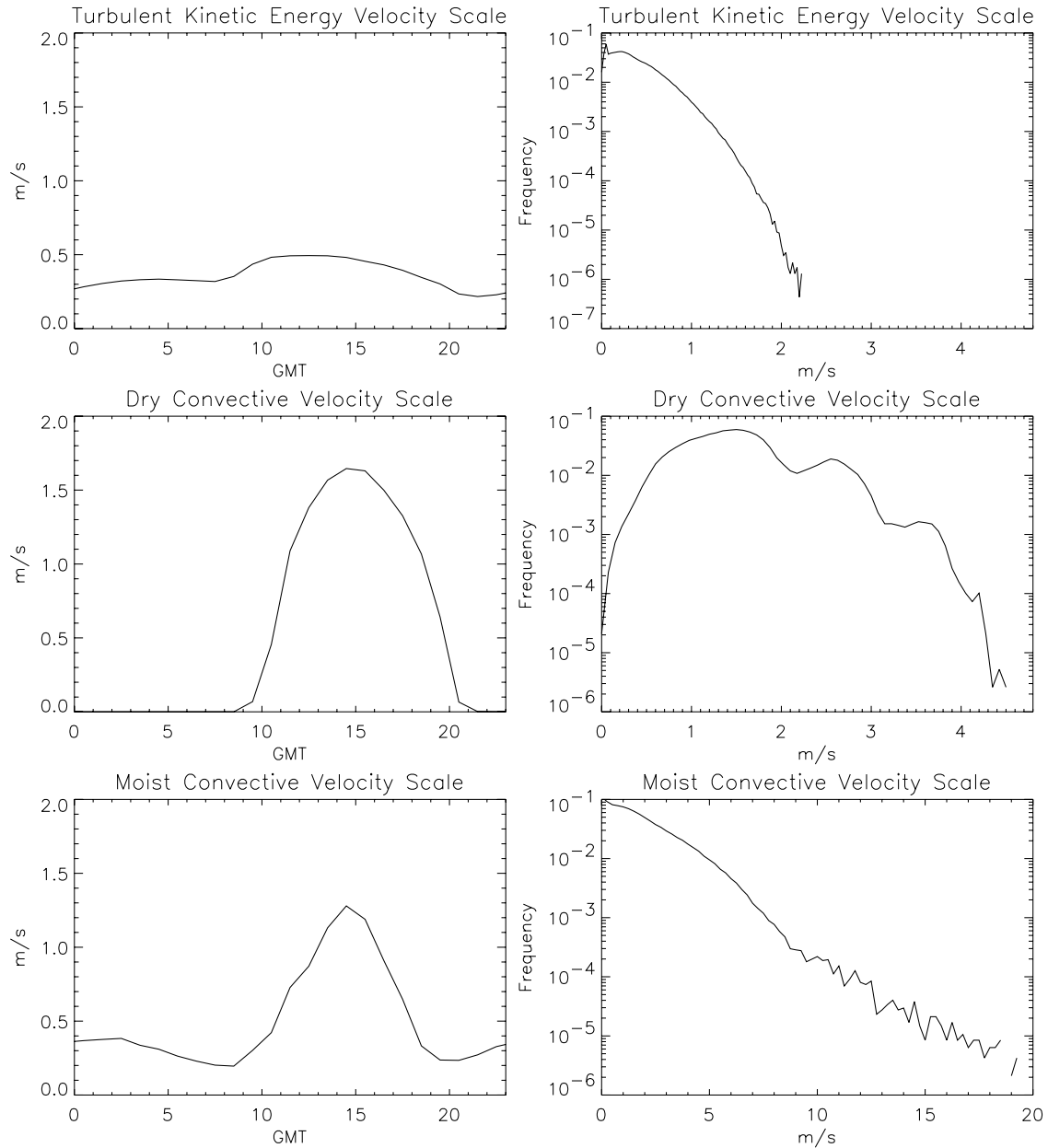


Figure 7. Average diurnal cycle during Northern Hemisphere summer of turbulent kinetic energy (TKE), dry, and moist (left) convective velocity scales over the Sahara and (right) their global frequency distribution. Note the different horizontal scale for the moist convective case.

convective downdrafts only within 5% of the grid box, consistent with our choice of σ_m in equation (9). The summertime diurnal cycle over Sahara (Figure 7, bottom), shows a peak in the moist convective scale in the early afternoon, similar to the cycle of dry convection. The moist convective scale is around 1 ms^{-1} , which is two times stronger than the TKE velocity scale but not as strong as the dry convective velocity scale. There are cases where w_m can exceed 15 ms^{-1} , in accordance with the observations described above. We plot the seasonal cycle of the dust emission when the moist convective velocity scale is used in Figure 8 (this experiment is hereafter referred to as the MOIST model). Note the similarity of the MOIST to the CONTROL experiment. Although they can have

much higher velocity scales than their dry convective counterparts, moist convective events over desert regions are rare and do not contribute much to the total emission (Figure 7).

5.4. Comparison to Observed AOT

[44] Here we compare the optical thickness in the CONTROL model with the different subgrid scale experiments. Figure 9 shows the three different subgrid scale simulations over regions dominated by mineral dust. In Figure 9, the thick solid black line is the DRY experiment, the solid gray line is the CONTROL, the dotted line is the TKE experiment, and the dash-dotted line is the MOIST model.

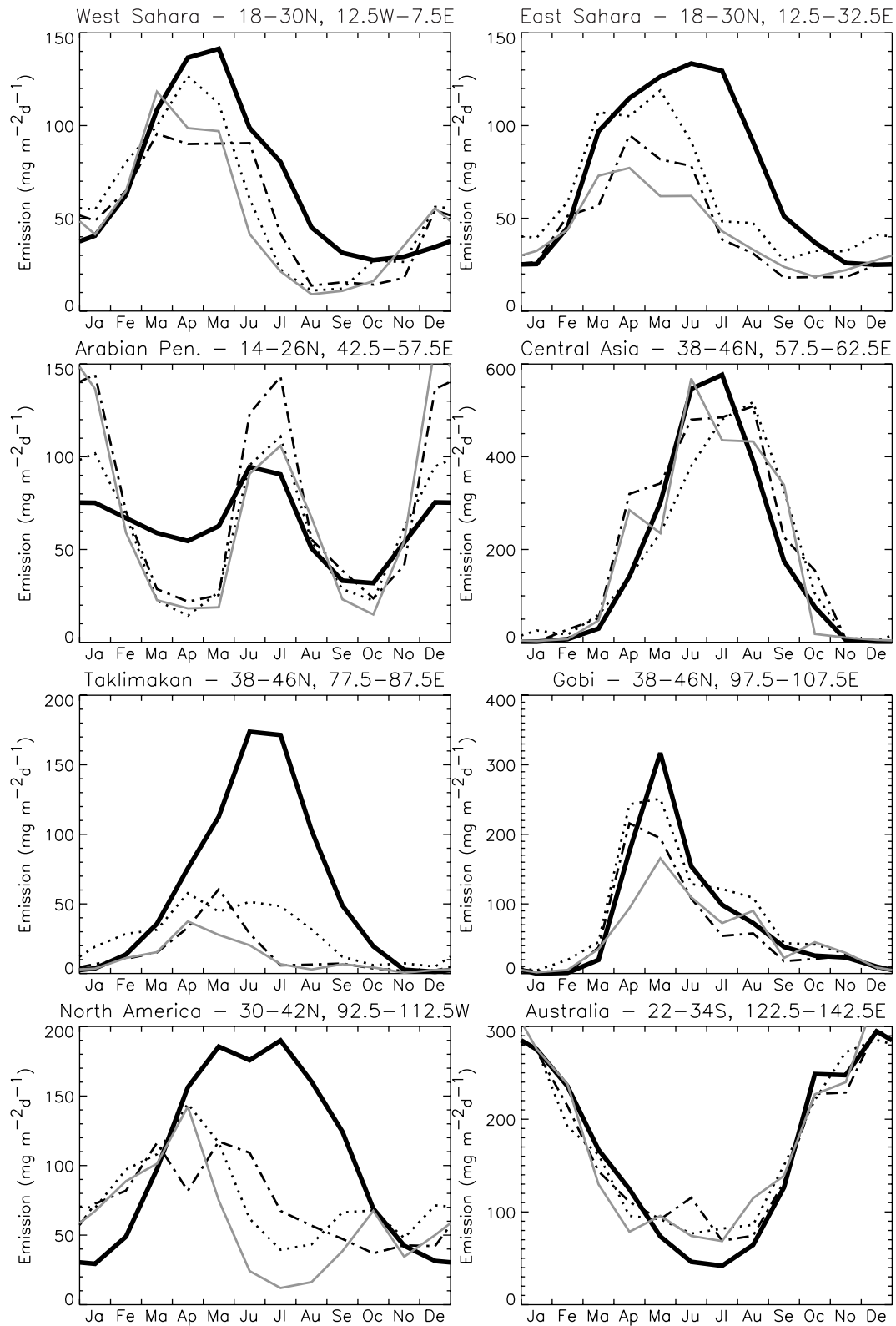


Figure 8. Regional averages of dust emission. The thick solid black line is the DRY experiment, the solid gray line is the CONTROL experiment, the dotted line is the TKE experiment, and the dash-dotted line is the MOIST experiment.

[45] Comparing the CONTROL and TKE experiments, there is practically no difference between the optical thicknesses over these specific regions. The source locations (not shown) are also similar. The inability of the PBL param-

eterization to improve the model optical thickness is probably due to the restriction of the PBL turbulence model to the bottom 200 m of the troposphere, missing contributions from deeper dry and moist convective eddies. Observations

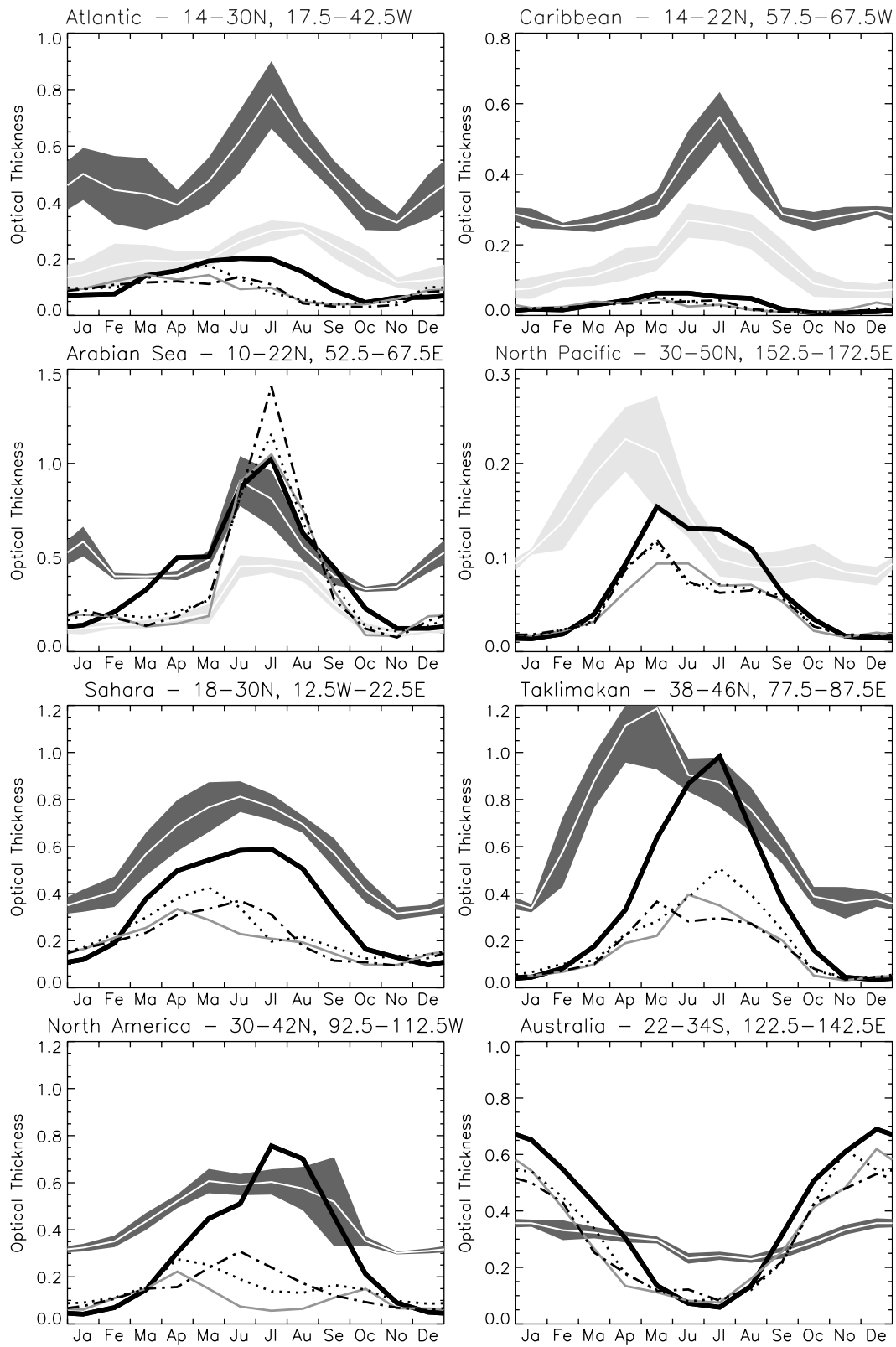


Figure 9. Regional averages of optical thickness. The thick solid black line is the DRY experiment, the dotted line is the TKE experiment, and the dash-dotted line is the MOIST experiment. The CONTROL experiment and satellite retrievals are as in Figure 1.

show that during the Northern Hemisphere summer, the atmosphere above the Saharan desert is dominated by a dry convective layer which extends to 5–6 km [Carlson and Prospero, 1972]. When we incorporate the effect of dry convection upon dust emission, there is general improvement in the optical thickness over the CONTROL model (Figure 9), especially during the Northern Hemisphere summer season over the Sahara and East Asia. In the MOIST experiment, there is barely any improvement compared to the CONTROL model.

6. Implementation of All Sources of Subgrid Variability

[46] In the previous section, we computed the individual contribution of each subgrid velocity scale to the dust distribution. In practice, the processes associated with each scale can occur simultaneously. This raises the question of how to combine the scales in order to compute the standard deviation σ of the total fluctuation: do the winds associated with each process reinforce each other, or are they uncorrelated? To consider two extreme cases, we combine fluctuations associated with each parameterization assuming either that they are totally independent of each other (e.g., $\sigma = \sqrt{w_p^2 + w_d^2 + w_m^2}$) or else perfectly correlated (e.g., $\sigma = w_p + w_d + w_m$), where w_p , w_d , and w_m are the velocity scales associated with the TKE, dry, and moist convection, respectively.

[47] When incorporating all three velocity scales, we raise w_t from 4 to 8 ms^{-1} . The higher threshold speed is motivated by the fact that in situ measurements of this threshold over the Sahara [Helgren and Prospero, 1987] and satellite-derived thresholds [Chomette et al., 1999] are around 8–10 ms^{-1} . We can now use the observed threshold, given the subgrid variance that allows wind speeds to exceed this threshold despite the limited AGCM resolution. The use of an identical emission threshold among all experiments might seem appropriate for evaluating the effects of subgrid wind variability. However, a CONTROL experiment with an 8 ms^{-1} threshold (not shown) is clearly unrealistic, with emission limited to the two locations with the highest surface winds: the Horn of Africa and Patagonia. In this case, improvement of the model AOT with the inclusion of subgrid variability is trivial. Conversely, use of a 4 ms^{-1} threshold given all three mechanisms of subgrid variability, results in emission that is unrealistically widespread and continual. By using different thresholds for the ALLSUBGRID and CONTROL experiments, we are tuning the latter to optimize its realism. This results in a more stringent criterion for improvement given the introduction of subgrid wind variations, than had we kept the threshold the same for all experiments.

[48] Figure 10 shows the optical thicknesses from different experiments. The thick solid black line assumes perfectly correlated fluctuations (hereafter, the ALLSUBGRID experiment); the dotted line assumes independent fluctuations (the SENSITIVITY 1 experiment), and the solid gray line is the CONTROL experiment. The correlated and independent experiments are nearly identical, and hereafter, we adopt the correlated form when combining these velocities. This choice is also consistent with the generally large and positive correlation between the velocity scales (not

shown). As a test of sensitivity, we repeated the simulations with $w_t = 10 \text{ ms}^{-1}$ and got a similar dust distribution compared to the case with $w_t = 8 \text{ ms}^{-1}$ (not shown).

[49] Figures 2 and 10 show that the inclusion of subgrid variations in surface wind speed improve the dust distribution compared to the CONTROL experiment. Figure 9 suggests that the main improvement in the model derives from the inclusion of dry convection as opposed to PBL TKE and moist convection. In fact, both the phase and the amplitude of the seasonal cycle of optical thickness of the ALLSUBGRID experiment resembles the experiment with only the dry convective velocity scale.

[50] During the Northern Hemisphere spring, the ALLSUBGRID experiment has greater optical thickness over the Sahara than the CONTROL model. In the Northern Hemisphere summer, the African dust plume extends farther over the subtropical North Atlantic Ocean by some 3000 km, although it is unable to reach the Caribbean basin. African waves have been shown by Jones et al. [2003] to contribute roughly 20% of Saharan emission during this season [see also Westphal et al., 1988]. Our AGCM underestimates African wave amplitude [Druyan and Hall, 1994], and this may contribute to insufficient transport to Barbados. Moreover, in experiments to be described elsewhere, we find that replacing the AGCM precipitation with the Climate Prediction Center (CPC) Merged Analysis of Precipitation (CMAP) retrievals results in a realistic seasonal cycle of dust AOT at Barbados, given subgrid variability in wind speed. This suggests that the AGCM overestimates wet deposition downwind of the African source. With the implementation of subgrid scale variability, the model is able to produce a more extensive SAL over the subtropical north Atlantic Ocean, as seen in Figure 4. The plume height is correctly modeled (800–600 mb), compared to the observations [Karyampudi et al., 1999]. As shown by the right panel of Figure 3, the plume is elevated farther above the surface, compared to the CONTROL run. The dust layer is still too diffuse in the vertical compared to observations [Karyampudi et al., 1999]. This may be associated with the AGCM's coarse vertical resolution, which is based upon nine layers in the troposphere. Nevertheless, emission by subgrid wind fluctuations contributes to increased realism of dust loading over the subtropical Atlantic Ocean.

[51] During both the Northern Hemisphere spring and summer, the ALLSUBGRID experiment has a higher optical thickness than the CONTROL over the Taklimakan and downwind over the North Pacific, in closer agreement with the satellite retrievals. The ALLSUBGRID experiment overestimates the summer dust load over Australia and North America, even though the annual average is correctly reproduced. However, the TOMS retrieval probably represents an upper bound on the dust AOT over North America. During Northern Hemisphere spring, soot aerosols created by biomass burning in Central America contribute to the TOMS retrieval. Furthermore, cloud contamination may bias the retrieved optical depth upward by as much as 0.1. Consequently, we believe the emission calculated by the AGCM over the US to be unrealistically large. During the summertime, dry convection is ubiquitous in these regions [Yamada and Mellor, 1975; Renno et al., 1998; Gillette, 1999]. While this favors emission, as shown by a comparison

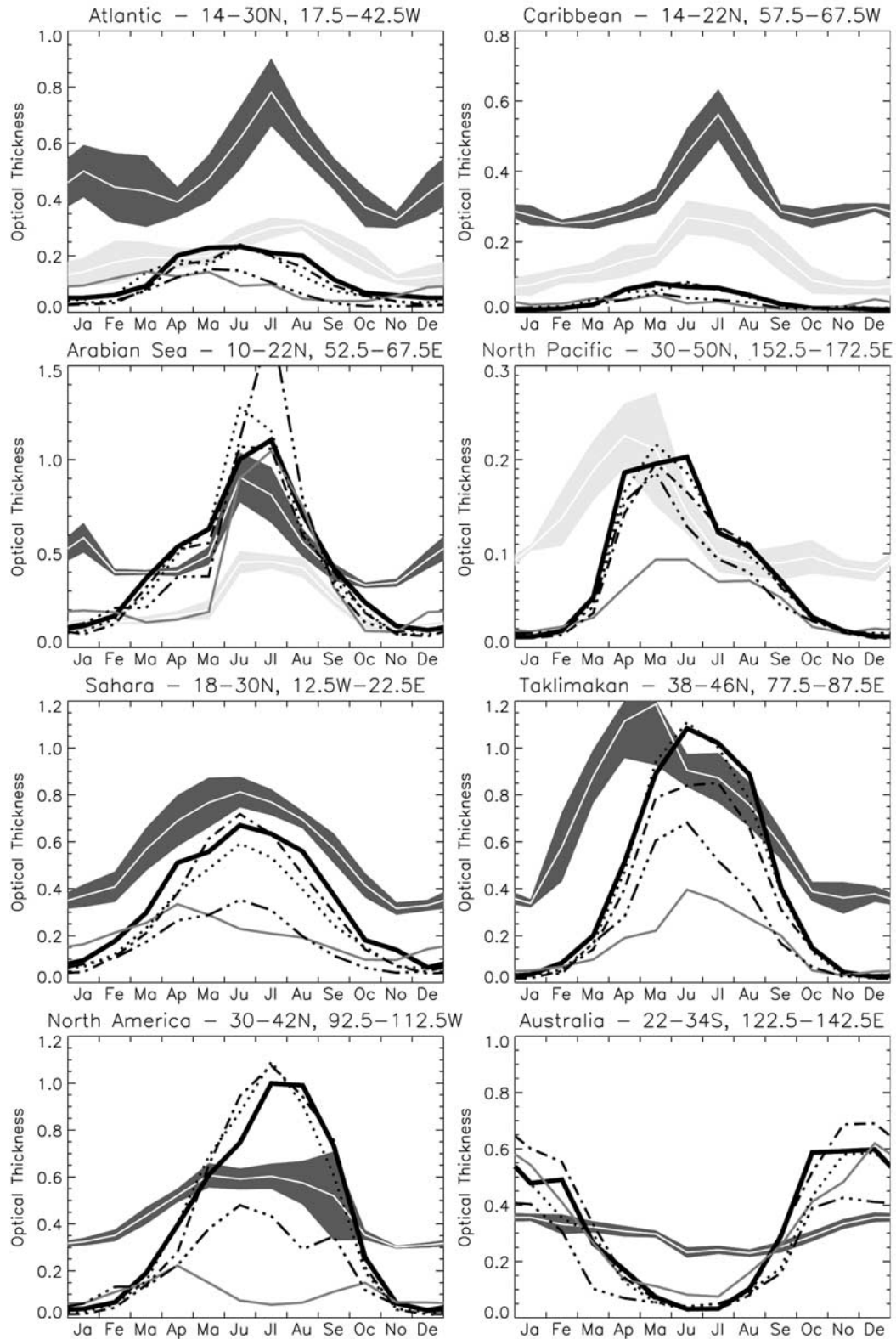


Figure 10. Regional averages of optical thickness. The thick solid black line is the ALLSUBGRID experiment, where the velocity scales add constructively ($\sigma = w_p + w_d + w_m$), the dotted line is where the velocity scales are assumed uncorrelated ($\sigma = \sqrt{w_p^2 + w_d^2 + w_m^2}$), the dash-dotted line is the ALLSUBGRID experiment without the TKE subgrid fluctuations, and the dash-triple-dotted line is where the velocity scales are added directly to the model-resolved mean wind speed. The CONTROL experiment and satellite retrievals are as in Figure 1.

of the ALLSUBGRID and CONTROL AOT in Figure 1, emission also depends upon the absence of vegetation and an abundance of erodible particles. Several studies show that emission over Australia is reduced by the introduction of preferred sources that identify regions of enhanced particle availability [Ginoux *et al.*, 2001; Tegen *et al.*, 2002; Zender *et al.*, 2003b]. However, other models do not show much dust emission over the American Southwest, even when availability of erodible particles is not accounted for [Zender *et al.*, 2003b]. This suggests that the unrealistically large emission of dust over the US by the AGCM is due to our specification of vegetation. We are currently considering alternative specifications.

[52] Despite identical global emission between the CONTROL and ALLSUBGRID experiments, the global mean optical thicknesses are 5.8 and 8.2, respectively. This large discrepancy can be explained by analyzing both the dry and wet deposition lifetime. Wet deposition depends not only upon the externally specified scavenging ratio, but also upon other factors, such as the meteorology of the AGCM and location of the source regions with respect to model rainfall. For instance, as we changed the model from CONTROL to ALLSUBGRID, the wet deposition lifetime increased from 9.1 to 11.6 days. In the CONTROL model, much of the Northern Hemisphere summertime emission occurs over the Horn of Africa, upwind from a region of high rainfall over the Arabian Sea. Therefore most of the dust emitted in the CONTROL experiment is immediately deposited into the ocean. This is in contrast to the ALLSUBGRID model, where dry convection increases emission over deserts far from precipitation. Hence the emitted dust particles must be transported great distances before they can be removed from the atmosphere by wet deposition. Similarly, mixing within the deep convective boundary layer over a desert carries dust particles high above the surface, far from the reach of dry deposition compared to a shallower boundary layer. We speculate this is the reason that the dry deposition lifetime in the ALLSUBGRID model lengthens from 7.2 to 11.1 days. These examples illustrate that subgrid circulations not only change the geographic distribution of emission, but increase the particle lifetime. The increase in both dry and wet deposition lifetimes shows the contribution of the AGCM's circulation to dust removal in addition to the effect of the externally prescribed variables such as the scavenging efficiency and Stokes velocity.

[53] Lunt and Valdes [2002] also incorporate subgrid variability into their calculation of dust emission. Although the approach is analogous, their technique is different. First, they ignore subgrid scale variability associated with TKE computed by their model's PBL parameterization. Boundary layer TKE can contribute roughly half or more of the total subgrid variability during the night hours (Figure 7). Just before the sunrise over the Sahara, the contribution to the total subgrid variability is 0.3 ms^{-1} , 0.0 ms^{-1} , and 0.2 ms^{-1} for TKE, along with dry and moist convection, respectively. However, due to the nonlinearity of dust emission, the subgrid contribution is dominated by dry convection during the day, because its value is much higher than the TKE wind speed. We tested the ALLSUBGRID model without the TKE contribution to the subgrid scale variability (the SENSITIVITY 2 experiment), and the results resemble the

ALLSUBGRID, as shown by the dash-dotted line in Figure 10. In practice, it is safe to ignore TKE as a contributor to the subgrid scale variability. (Note that over North America, the Sahara, and Australia, the experiment without TKE has a higher optical depth than the ALLSUBGRID model. This can result from our constraint that global emission be identical in the two experiments: an emission reduction in one region, due to the absence of TKE in calculating subgrid variability, is necessarily balanced by an increase elsewhere.)

[54] To calculate emission, Lunt and Valdes [2002] follow Miller *et al.* [1992], augmenting the speed of the resolved model wind, \bar{w} with their subgrid velocity scales. In contrast, we introduce them through the standard deviation of the wind speed distribution of equation (6). In order to test the significance of such a difference, we adopted their approach (the SENSITIVITY 3 experiment), shown as the dash-triple-dotted line in Figure 10. Comparing the latter to ALLSUBGRID shows that our incorporation of these subgrid speeds as the standard deviation helps us emit more dust over the Sahara, subsequently resulting in greater transport over the Atlantic Ocean. Lunt and Valdes [2002] also apply the moist convective downdraft over a whole model grid box (whose dimension is a few hundred of kilometers), even though these winds typically happen over a much smaller area. Their moist convective velocity scale is derived from observations of oceanic surface precipitation [Redelsperger, 2000; Jabouille *et al.*, 1996], over the Tropical Ocean Global Atmosphere (TOGA) Coupled Ocean-Atmosphere Response Experiment (COARE) array, as well as results from a cloud-resolving model. This parameterization allows maximum speeds of about 3 ms^{-1} . Although this is a reasonable value of gustiness when averaged over the whole model grid box, dust emission may be different for smaller scale but more intense wind bursts. We model the emission using high wind speeds within a fraction of the grid box instead of applying lower wind speeds to the entire grid box. However, we find in practice that moist convection contributes relatively little to dust emission due to the high soil moisture in most convecting regions (Figure 9), so that the distinction is moot.

[55] In contrast to our results, Lunt and Valdes [2002] find that emission is very sensitive to whether fluctuations associated with the different velocity scales are correlated or independent with emission, increasing by nearly a factor of two in the former case. This sensitivity can be attributed to their holding C constant in the two experiments, and the fact that $\bar{w} + w_d + w_m$ is necessarily greater than $\sqrt{\bar{w}^2 + w_d^2 + w_m^2}$. In contrast, we vary C to hold the global emission fixed (Figure 10). In this case, we find that the geographic distribution of optical thickness of dust is insensitive to our choice of correlated as opposed to independent fluctuations.

7. Conclusions

[56] The original parameterization of dust in the GISS AGCM [Tegen and Miller, 1998] uses a horizontally varying threshold speed adjusted based upon emission calculated off-line with higher resolution surface wind reanalyses. The new parameterization of subgrid wind speed variability

eliminates these “tuning knobs” and restores a globally uniform threshold speed. The AGCM overcomes its limited spatial resolution to simulate a realistic dust distribution by accounting for subgrid wind speed fluctuations using information from the PBL and convective parameterizations. Although the original thresholds were tuned ostensibly to indicate regions of large subgrid variability identified by the reanalyses, this variability is now calculated based upon a physical parameterization and can evolve with the model meteorology. As a result, the modeled optical thickness is much closer to observations provided by the TOMS and AVHRR retrievals. Most of the improvement comes from subgrid fluctuations associated with dry convection due to solar heating over arid surfaces. This not only changes emission but increases the aerosol lifetime (and thus the load). Particles emitted from an arid region originate farther upwind of precipitation and are mixed higher above the surface, farther from the reach of dry deposition.

[57] Both the Asian and the African dust plumes extend farther downwind in the ALLSUBGRID experiment due to increased emission by subgrid wind fluctuations in the source regions. However, the African dust plume is still unable to reach the Caribbean basin, probably because of excessive AGCM rainfall over the subtropical Atlantic Ocean and Sahara.

[58] By parameterizing subgrid wind variability using information from the AGCM, we are able to remove hundreds of tuning knobs from the original AGCM dust parameterization that included horizontal variations in threshold speed [Tegen and Miller, 1998]. To be sure, a handful of tunable parameters remain in the ALLSUBGRID model. Because each velocity scale represents only the order of magnitude of subgrid wind fluctuations due to TKE along with dry and moist convection, they can be multiplied by factors of order unity (and thus tuned) while remaining consistent with observations. Nonetheless, the ALLSUBGRID experiment indicates the value of allowing the model to identify meteorology preferential to dust emission. The subgrid wind parameterization can be applied to any wind-blown aerosol, even if the flux has a different dependence upon wind speed. It is currently being used to simulate emission of dimethylsulfide and sea salt (D. Koch, personal communication, 2003).

[59] Despite more realistic simulation of AOT with the inclusion of subgrid wind variability, excessive emission persists over Australia and is exacerbated over the American Southwest. The model’s overestimate of summertime emission over Australia suggests a consideration of soil erodibility, which has led to better simulations in other models [Ginoux *et al.*, 2001; Tegen *et al.*, 2002; Zender *et al.*, 2003b]. Given that preferred source locations (generally corresponding to dry lake beds) are colocated under the “hot spots” of dust emission identified by TOMS [Prospero *et al.*, 2002], we expect to reproduce the TOMS observations more closely after including these sources. Over the southwest US, our AGCM calculates emission that is excessive compared to other models, even those without preferred sources [Zender *et al.*, 2003b]. The unrealistic emission is exacerbated by the frequent dry convection in this region during this season [Renno *et al.*, 1998; Gillette, 1999]. It is unclear why the southwest US is not a larger source of atmospheric dust. The region is generally arid,

with sparse vegetation, and abundant dry lake beds, conditions that are believed to favor dust emission elsewhere [Prospero *et al.*, 2002]. We are currently experimenting with preferred sources (to complement our parameterization of “preferred meteorology”), along with a new representation of vegetation; the latter has reduced emission over North America to more realistic levels. Excessive emission by the AGCM over North America shows the importance of correctly specifying the surface properties (including vegetation and the availability of erodible particles) not only in regions of high surface winds but in regions where dry convection is ubiquitous and the surface winds are highly variable.

[60] The mechanistic representation of subgrid wind variability allows us to calculate changes in dust emission by small-scale circulations outside the current climate, due to anthropogenic CO₂, for example. In our simulation of the current climate, emission associated with subgrid wind fluctuations is dominated by dry convection. With an increase of radiation into the surface due to CO₂, there will be a greater surface sensible heat flux back into the atmosphere and more vigorous dry convection. This will cause an increase in dust emission. The increase in radiative heating of the surface by CO₂ will also increase evaporation from the surface, thus increasing precipitation and removal of dust from the atmosphere by wet deposition. Increased precipitation can decrease dust emission by increasing the soil moisture. The net effect upon the dust burden by these competing processes remains to be calculated.

[61] **Acknowledgments.** We are grateful to Mark Cane, Lorenzo Polvani, Bill Rossow, Adam Sobel, and two anonymous reviewers for their useful comments and suggestions. We also thank Larry Stowe for providing the AVHRR retrieval and guidance concerning its use and Lilly Del Valle for drafting a figure. This work was supported by the Climate Dynamics Program of the National Science Foundation through grant ATM-01-24258.

References

- Abramowitz, M., and I. Stegun (1985), *Handbook of Mathematical Functions With Formulas, Graphs, and Mathematical Tables*, 10th ed., John Wiley, Hoboken, N. J.
- Ahrens, C. D. (1994), *Meteorology Today: An Introduction to Weather, Climate and the Environment*, 5th ed., West Publ., New York.
- Alfaro, S. C., A. Gaudichet, L. Gomes, and M. Maillé (1997), Modeling the size distribution of a soil aerosol produced by sandblasting, *J. Geophys. Res.*, **102**, 11,239–11,249.
- Arya, S. P. (1988), *Introduction to Micrometeorology*, Int. Geophys. Ser., vol. 42, Academic, San Diego, Calif.
- Bagnold, R. (1941), *The Physics of Blown Sand and Desert Dunes*, Methuen, New York.
- Cakmur, R. V. (2003), Mineral dust variability and the parameterization of emission due to unresolved circulations, Ph.D. thesis, Columbia Univ., New York.
- Canuto, V. M., F. Minotti, C. Ronchi, and R. M. Ypma (1994), Second-order closure PBL model with new third-order moments: Comparison with LES data, *J. Atmos. Sci.*, **51**, 1605–1618.
- Carlin, J., and J. Haslett (1982), The probability distribution of wind power from a dispersed array of wind turbine generators, *J. Appl. Meteorol.*, **21**, 303–313.
- Carlson, T. N., and J. M. Prospero (1972), The large-scale movement of Saharan air outbreaks over the northern equatorial Atlantic, *J. Appl. Meteorol.*, **11**, 283–297.
- Caughey, S. J., and S. G. Palmer (1979), Some aspects of turbulence structure through the depth of the convective boundary layer, *Q. J. R. Meteorol. Soc.*, **105**, 811–827.
- Caughey, S. J., and C. J. Readings (1975), Turbulent fluctuations in convective conditions, *Q. J. R. Meteorol. Soc.*, **101**, 537–542.
- Cheng, Y., V. M. Canuto, and A. M. Howard (2002), An improved turbulence model for the turbulent PBL, *J. Atmos. Sci.*, **59**, 1550–1565.

- Chiapello, I., P. Goloub, D. Tanré, A. Marchand, J. Herman, and O. Torres (2000), Aerosol detection by TOMS and POLDER over oceanic regions, *J. Geophys. Res.*, **105**, 7133–7142.
- Chomette, O., M. Legrand, and B. Marticorena (1999), Determination of the wind speed threshold for the emission of desert dust using satellite remote sensing in the thermal infrared, *J. Geophys. Res.*, **104**, 31,207–31,215.
- Christofferson, R. (1987), A simple estimator of the shape factor of the two-parameter Weibull distribution, *J. Clim. Appl. Meteorol.*, **26**, 323–325.
- Conradsen, K., L. Nielsen, and L. Prahm (1984), Review of Weibull statistics for estimation of wind speed distributions, *J. Clim. Appl. Meteorol.*, **23**, 1173–1183.
- Deardorff, J. W. (1974), Three-dimensional numerical study of turbulence in an entraining mixed layer, *Boundary Layer Meteorol.*, **7**, 199–226.
- Del Genio, A. D., and M. S. Yao (1988), Sensitivity of a global climate model to the specification of convective updraft and downdraft mass fluxes, *J. Atmos. Sci.*, **45**, 2641–2668.
- Del Genio, A. D., and M. S. Yao (1993), *The Representation of Cumulus Convection in Numerical Models*, Meteorol. Monogr. Ser., vol. 24, pp. 181–184, Am. Meteorol. Soc., Boston, Mass.
- Del Genio, A., M. Yao, W. Kovari, and K. Lo (1996), A prognostic cloud water parameterization for global climate models, *J. Clim.*, **9**, 270–304.
- Druyan, L., and T. Hall (1994), Studies of African wave disturbances with the GISS GCM, *J. Clim.*, **7**, 261–276.
- Duce, R. (1995), Sources, distributions, and fluxes of mineral aerosols and their relationship to climate change, in *Dahlem Workshop on Aerosol Forcing of Climate*, Environ. Sci. Res. Rep. 17, edited by R. J. Charlson and J. Heintzenber, pp. 43–72, John Wiley, Hoboken, N. J.
- Emanuel, K. A., and M. Z. Rothman (1999), Development and evaluation of a convection scheme for use in climate models, *J. Atmos. Sci.*, **56**, 1766–1782.
- Engelstaedt, S., K. E. Kohfeld, I. Tegen, and S. P. Harrison (2003), Controls of dust emissions by vegetation and topographic depressions: An evaluation using dust storm frequency data, *Geophys. Res. Lett.*, **30**(6), 1294, doi:10.1029/2002GL016471.
- Freund, J. E., and R. E. Walpole (1987), *Mathematical Statistics*, 4th ed., Prentice-Hall, Old Tappan, N. J.
- Gardner, W. R. (1983), Soil properties and efficient water use, in *Limitations to Efficient Water Use in Crop Production*, edited by T. R. S. H. M. Taylor and W. R. Jordan, Am. Soc. of Agron., Madison, Wis.
- Gillette, D. (1978), A wind tunnel simulation of the erosion of soil: Effect of soil texture, sandblasting, wind speed, and soil consolidation on dust production, *Atmos. Environ.*, **12**, 1735–1743.
- Gillette, D. A. (1999), A qualitative geophysical explanation for “hot spot” dust emitting source regions, *Contrib. Atmos. Phys.*, **72**, 67–77.
- Gillette, D. A., and R. Passi (1988), Modeling dust emission caused by wind erosion, *J. Geophys. Res.*, **93**, 14,233–14,242.
- Ginoux, P., M. Chin, I. Tegen, J. M. Prospero, B. Holben, O. Dubovik, and S.-J. Lin (2001), Sources and distributions of dust aerosols simulated with the GOCART model, *J. Geophys. Res.*, **106**, 20,255–20,273.
- Gomes, L., G. Bergametti, G. Coudé-Gaussen, and P. Rognon (1990), Submicron desert dusts: A sandblasting process, *J. Geophys. Res.*, **95**, 13,927–13,935.
- Guelle, W., Y. J. Balkanski, M. Schulz, B. Marticorena, G. Bergametti, C. Moulin, R. Arimoto, and K. D. Perry (2000), Modeling the atmospheric distribution of mineral aerosol: Comparison with ground measurements and satellite observations for yearly and synoptic time-scales over the North Atlantic, *J. Geophys. Res.*, **105**, 1997–2012.
- Hammond, A. L., (Ed.) (1992), *World Resources 1992–1993*, Oxford Univ. Press, New York.
- Hansen, J., G. Russell, D. Rind, P. Stone, A. Lacis, S. Lebedeff, R. Ruedy, and L. Travis (1983), Efficient three-dimensional global models for climate studies: Models i and ii, *Mon. Weather Rev.*, **111**, 609–662.
- Hansen, J., et al. (1997), Forcings and chaos in interannual to decadal climate change, *J. Geophys. Res.*, **102**, 25,679–25,720.
- Hartke, G. J., and D. Rind (1997), Improved surface and boundary layer models for the Goddard Institute for Space Studies general circulation model, *J. Geophys. Res.*, **102**, 16,407–16,422.
- Helgren, D., and J. Prospero (1987), Wind velocities associated with dust deflation events in the western Sahara, *J. Clim. Appl. Meteorol.*, **26**, 1147–1151.
- Herman, J. R., P. K. Bhartia, O. Torres, C. Hsu, C. Seftor, and E. Celarier (1997), Global distribution of UV-absorbing aerosols from Nimbus 7/TOMS data, *J. Geophys. Res.*, **102**, 16,911–16,922.
- Hess, G., and K. Spillane (1990), Characteristics of dust devils in Australia, *J. Appl. Meteorol.*, **29**, 498–507.
- Houze, R. A., Jr., and A. K. Betts (1981), Convection in GATE, *Rev. Geophys.*, **19**, 541–576.
- Husar, R. B., J. M. Prospero, and L. L. Stowe (1997), Characterization of tropospheric aerosols over the oceans with the NOAA advanced very high resolution radiometer optical thickness operational product, *J. Geophys. Res.*, **102**, 16,889–16,909.
- Idso, S. B. (1974), Tornado or dust devil: The enigma of desert whirlwinds, *Am. Sci.*, **62**, 530–541.
- Idso, S. B., R. S. Ingram, and J. M. Pritchard (1972), An american haboob, *Bull. Am. Meteorol. Soc.*, **53**, 930–935.
- Idso, S. W. (1976), Dust storms, *Sci. Am.*, **235**, 108–114.
- Iversen, J., and B. White (1982), Saltation threshold on Earth, Mars and Venus, *Sedimentology*, **29**, 111–119.
- Jabouille, P., J. L. Redelsperger, and J. P. Lafore (1996), Modification of surface fluxes by atmospheric convection in the TOGA COARE region, *Mon. Weather Rev.*, **124**, 816–837.
- Jones, C., N. Mahowald, and C. Luo (2003), The role of easterly waves on African desert dust transport, *J. Clim.*, **16**, 3617–3628.
- Justus, C. G., and A. Mikhail (1976), Height variation of wind speed and wind distributions statistics, *Geophys. Res. Lett.*, **3**, 261–264.
- Karyampudi, V., and T. Carlson (1988), Analysis and numerical simulations of the Saharan air layer and its effects on Easterly wave disturbances, *J. Atmos. Sci.*, **45**, 3102–3136.
- Karyampudi, V., et al. (1999), Validation of the Saharan dust plume conceptual model using lidar, meteorostat, and ECMWF data, *Bull. Am. Meteorol. Soc.*, **80**, 1045–1075.
- Lawson, T. J. (1971), Haboob structure at Khartoum, *Weather*, **26**, 105–112.
- Lenschow, D. H., and P. L. Stephens (1980), The role of thermals in the convective boundary layer, *Boundary Layer Meteorol.*, **19**, 509–532.
- Léon, J.-F., and M. Legrand (2003), Mineral dust sources in the surroundings of the north Indian Ocean, *Geophys. Res. Lett.*, **30**(6), 1309, doi:10.1029/2002GL016690.
- Leovy, C. B. (2003), The devil is in the dust, *Nature*, **424**, 1008–1009.
- Lu, H., and Y. Shao (1999), A new model for dust emission by saltation bombardment, *J. Geophys. Res.*, **104**, 16,827–16,842.
- Lunt, D. J., and P. J. Valdes (2002), The modern dust cycle: Comparison of model results with observations and study of sensitivities, *J. Geophys. Res.*, **107**(D23), 4669, doi:10.1029/2002JD002316.
- Mahowald, N., K. Kohfeld, M. Hansson, Y. Balkanski, S. P. Harrison, I. C. Prentice, M. Schulz, and H. Rodhe (1999), Dust sources and deposition during the Last Glacial Maximum and current climate: A comparison of model results with paleodata from ice cores and marine sediments, *J. Geophys. Res.*, **104**, 15,895–15,916.
- Mahowald, N. M., C. S. Zender, C. Luo, D. Savoie, O. Torres, and J. del Corral (2002), Understanding the 30-year Barbados desert dust record, *J. Geophys. Res.*, **107**(D21), 4561, doi:10.1029/2002JD002097.
- Mahowald, N., C. Luo, J. del Corral, and C. S. Zender (2003), Interannual variability in atmospheric mineral aerosols from a 22-year model simulation and observational data, *J. Geophys. Res.*, **108**(D12), 4352, doi:10.1029/2002JD002821.
- Marengo, J. A., and L. M. Druyan (1994), Validation of model improvements for the GISS GCM, *Clim. Dyn.*, **10**, 163–179.
- Marticorena, B., and G. Bergametti (1995), Modeling the atmospheric dust cycle: 1. Design of a soil-derived dust emission scheme, *J. Geophys. Res.*, **100**, 16,415–16,430.
- Matthews, E. (1983), Global vegetation and land use: New high-resolution databases for climate studies, *J. Clim. Appl. Meteorol.*, **22**, 474–487.
- Mellor, G. L., and T. Yamada (1982), Development of a turbulence closure model for geophysical fluid problems, *Rev. Geophys.*, **20**, 851–875.
- Middleton, N. J., and D. S. G. Thomas (1992), *World Atlas of Desertification*, John Wiley, Hoboken, N. J.
- Miller, M. J., A. C. M. Beljaars, and T. N. Palmer (1992), The sensitivity of the ECMWF model to the parameterization of evaporation from the tropical oceans, *J. Clim.*, **5**, 418–434.
- Miller, R. L., and A. Del Genio (1994), Tropical cloud feedbacks and natural variability of climate, *J. Clim.*, **7**, 1388–1402.
- Miller, R. L., and I. Tegen (1998), Climate response to soil dust aerosols, *J. Clim.*, **11**, 3247–3267.
- Miller, R. L., I. Tegen, and J. Perlwitz (2004), Surface radiative forcing by soil dust aerosols and the hydrologic cycle, *J. Geophys. Res.*, **109**, doi:10.1029/2003JD004085, in press.
- Morales, C. (1986), The airborne transport of Saharan dust: A review, *Clim. Change*, **9**, 219–241.
- Myhre, G., et al. (2004), Intercomparison of satellite retrieved aerosol optical depth over ocean, *J. Atmos. Sci.*, **61**, 499–513.
- Newman, C. E., S. R. Lewis, P. L. Read, and F. Forget (2002), Modeling the Martian dust cycle: 1. Representations of dust transport processes, *J. Geophys. Res.*, **107**(E12), 5123, doi:10.1029/2002JE001910.
- Panofsky, H. A., H. Tennekes, D. H. Lenschow, and J. C. Wyngaard (1977), The characteristics of turbulent velocity components in the surface layer under convective conditions, *Boundary Layer Meteorol.*, **11**, 355–361.
- Pavia, E., and J. O'Brien (1986), Weibull statistics of wind speed over the ocean, *J. Clim. Appl. Meteorol.*, **25**, 1324–1332.

- Perlwitz, J., I. Tegen, and R. L. Miller (2001), Interactive soil dust aerosol model in the GISS GCM: 1. Sensitivity of the soil dust cycle to radiative properties of soil dust aerosols, *J. Geophys. Res.*, **106**, 18,167–18,192.
- Prather, M. J. (1986), Numerical advection by conservation of second-order moments, *J. Geophys. Res.*, **91**, 6671–6681.
- Press, W., S. Teukolsky, W. Vetterling, and B. Flannery (1996), *Numerical Recipes in Fortran 77*, vol. 1, Cambridge Univ. Press, New York.
- Prospero, J. M., P. Ginoux, O. Torres, S. E. Nicholson, and T. E. Gill (2002), Environmental characterization of global sources of atmospheric soil dust identified with the Nimbus 7 Total Ozone Mapping Spectrometer (TOMS) absorbing aerosol product, *Rev. Geophys.*, **40**(1), 1002, doi:10.1029/2000RG000095.
- Reader, M. C., I. Fung, and N. McFarlane (1999), The mineral dust aerosol cycle during the Last Glacial Maximum, *J. Geophys. Res.*, **104**, 9381–9398.
- Redelsperger, J. L. (2000), A parameterization of mesoscale enhancement of surface fluxes for large-scale models, *J. Clim.*, **13**, 402–421.
- Renno, N., M. Burkett, and M. Larkin (1998), A simple thermodynamical theory of dust devils, *J. Atmos. Sci.*, **55**, 3244–3252.
- Schulz, M., Y. J. Balkanski, W. Guelle, and F. Dulac (1998), Role of aerosol size distribution and source location in a three-dimensional simulation of a Saharan dust episode tested against satellite-derived optical thickness, *J. Geophys. Res.*, **103**, 10,579–10,592.
- Shao, Y., M. R. Raupach, and P. A. Findlater (1993), Effect of saltation bombardment on the entrainment of dust by wind, *J. Geophys. Res.*, **98**, 12,719–12,726.
- Shao, Y., M. R. Raupach, and J. F. Leys (1996), A model for predicting aeolian sand drift and dust entrainment on scales from paddock to region, *Aust. J. Soil Res.*, **34**, 309–342.
- Sinclair, P. C. (1973), The lower structure of dust devils, *J. Atmos. Sci.*, **30**, 1599–1619.
- Stull, R. B. (1988), *An Introduction to Boundary-Layer Meteorology*, Kluwer Acad., Norwell, Mass.
- Takemura, T., H. Okamoto, Y. Maruyama, A. Numaguti, A. Higurashi, and T. Nakajima (2000), Global three-dimensional simulation of aerosol optical thickness distribution of various origins, *J. Geophys. Res.*, **105**, 17,853–17,873.
- Tegen, I., and I. Fung (1994), Modeling of mineral dust in the atmosphere: Sources, transport, and optical thickness, *J. Geophys. Res.*, **99**, 22,897–22,914.
- Tegen, I., and A. A. Lacis (1996), Modeling of particle size distribution and its influence on the radiative properties of mineral dust aerosol, *J. Geophys. Res.*, **101**, 19,237–19,244.
- Tegen, I., and R. L. Miller (1998), A general circulation model study on the interannual variability of soil dust aerosol, *J. Geophys. Res.*, **103**, 25,975–25,995.
- Tegen, I., A. A. Lacis, and I. Fung (1996), The influence on climate forcing of mineral aerosols from disturbed soils, *Nature*, **380**, 419–422.
- Tegen, I., P. Hollrig, M. Chin, I. Fung, D. Jacob, and J. Penner (1997), Contribution of different aerosol species to the global aerosol extinction optical thickness: Estimates from model results, *J. Geophys. Res.*, **102**, 23,895–23,915.
- Tegen, I., S. P. Harrison, K. Kohfeld, I. C. Prentice, M. Coe, and M. Heimann (2002), Impact of vegetation and preferential source areas on global dust aerosol: Results from a model study, *J. Geophys. Res.*, **107**(D21), 4576, doi:10.1029/2001JD000963.
- Torres, O., P. K. Bhartia, J. R. Herman, A. Sinyuk, P. Ginoux, and B. Holben (2002), A long-term record of aerosol optical depth from TOMS observations and comparison to AERONET measurements, *J. Atmos. Sci.*, **59**, 398–413.
- Tucker, C., H. Dregne, and W. Newcomb (1991), Expansion and contraction of the Sahara desert from 1980 to 1990, *Science*, **253**, 299–301.
- Webb, R., C. Rosenzweig, and E. R. Levine (1991), A global data set of particle size properties, *Tech. Rep. TM-4286*, 33 pp., NASA, New York.
- Westphal, D. L., O. B. Toon, and T. N. Carlson (1988), A case study of mobilization and transport of Saharan dust, *J. Atmos. Sci.*, **45**, 2145–2175.
- Willis, G. E., and J. W. Deardorff (1974), A laboratory model of the unstable planetary boundary layer, *J. Atmos. Sci.*, **31**, 1297–1307.
- Wyngaard, J. C. (1985), Structure of the planetary boundary layer and implications for its modeling, *J. Clim. Appl. Meteorol.*, **24**, 1131–1142.
- Wyngaard, J. C., and O. R. Cote (1974), The evolution of a convective planetary boundary layer—A higher-order-closure model study, *Boundary Layer Meteorol.*, **7**, 289–308.
- Yamada, T., and G. Mellor (1975), A simulation of the Wangara atmospheric boundary layer data, *J. Atmos. Sci.*, **32**, 2309–2329.
- Zender, C. S., H. Bian, and D. Newman (2003a), Mineral Dust Entrainment and Deposition (DEAD) model: Description and 1990s dust climatology, *J. Geophys. Res.*, **108**(D14), 4416, doi:10.1029/2002JD002775.
- Zender, C. S., D. Newman, and O. Torres (2003b), Spatial heterogeneity in aeolian erodibility: Uniform, topographic, geomorphic, and hydrologic hypotheses, *J. Geophys. Res.*, **108**(D17), 4543, doi:10.1029/2002JD003039.
- Zhang, X., R. Arimoto, G. Zhu, T. Chen, and G. Zhang (1998), Concentration, size-distribution and deposition of mineral aerosol over Chinese desert regions, *Tellus, Ser. B*, **50**, 317–330.
- Zobler, L. (1986), A world soil file for global climate modeling, *Tech. Rep. TM-87802*, 32 pp., NASA, New York.

R. V. Cakmur, Department of Applied Physics and Applied Mathematics, Columbia University, 200 S. W. Mudd Building, 500 West 120th Street, New York, NY 10027, USA. (rcakmur@giss.nasa.gov)

R. L. Miller, NASA Goddard Institute for Space Studies, 2880 Broadway, New York, NY 10025, USA. (rmiller@giss.nasa.gov)

O. Torres, Joint Center for Earth Systems Technology, University of Maryland Baltimore County, Academic IV, A-wing Room 114, 1000 Hilltop Circle, Baltimore, MD 21250, USA. (torres@tparty.gsfc.nasa.gov)